

GraphPerf-RT: A Graph-Driven Performance Model for Hardware-Aware Scheduling of OpenMP Codes

Mohammad Pivezhandi¹, Mahdi Banisharif², Saeed Bakhshani¹, Abusayeed Saifullah³, and Ali Jannesari²

¹Wayne State University

²Iowa State University

³The University of Texas at Dallas

Abstract

Performance prediction for OpenMP workloads on heterogeneous embedded SoCs is challenging due to complex interactions between task DAG structure, control-flow irregularity, cache and branch behavior, and thermal dynamics; classical heuristics struggle under workload irregularity, tabular regressors discard structural information, and model-free RL risks overheating resource-constrained devices. We introduce GraphPerf-RT, the first surrogate that unifies task DAG topology, CFG-derived code semantics, and runtime context (per-core DVFS, thermal state, utilization) in a heterogeneous graph representation with typed edges encoding precedence, placement, and contention. Multi-task evidential heads predict makespan, energy, cache and branch misses, and utilization with calibrated uncertainty (Normal-Inverse-Gamma), enabling risk-aware scheduling that filters low-confidence rollouts. We validate GraphPerf-RT on three embedded ARM platforms (Jetson TX2, Jetson Orin NX, RUBIK Pi), achieving $R^2 > 0.95$ with well-calibrated uncertainty ($ECE < 0.05$). To demonstrate end-to-end scheduling utility, we integrate the surrogate with four RL methods on Jetson TX2: single-agent model-free (SAM-FRL), single-agent model-based (SAMBRL), multi-agent model-free (MAMFRL-D3QN), and multi-agent model-based (MAMBRL-D3QN). Experiments across 5 seeds (200 episodes each) show that MAMBRL-D3QN with GraphPerf-RT as the world model achieves 66% makespan reduction (0.97 ± 0.35 s) and 82% energy reduction (0.006 ± 0.005 J) compared to model-free baselines, demonstrating that accurate, uncertainty-aware surrogates enable effective model-based planning on thermally constrained embedded systems.

1 Introduction

Heterogeneous embedded Systems-on-Chip (SoCs) combine high-performance and energy-efficient cores with Dynamic Voltage and Frequency Scaling (DVFS). This architecture has created unprecedented opportunities for deploying parallel applications in resource-constrained environments such as autonomous vehicles, robotics, and edge computing. OpenMP, the dominant shared-memory parallel programming model, enables developers to express task-level parallelism through pragma-based annotations that the runtime system maps to available hardware resources. However, achieving optimal performance on these heterogeneous platforms requires careful scheduling decisions that balance execution time, energy efficiency, and thermal constraints. This presents a challenging optimization problem that current approaches fail to address comprehensively. Performance prediction for parallel workloads has traditionally relied on analytical models, simulation-based methods, and machine learning surrogates. Analytical models grounded in queueing theory and scheduling

bounds such as Brent’s theorem provide theoretical insights but require simplifying assumptions that break down under irregular control flow and cache contention (Graham, 1969; Brent, 1974). Simulation-based approaches offer high fidelity but incur prohibitive runtime overhead for online scheduling decisions. Machine learning surrogates, including Graph Neural Networks (GNNs), can learn complex input-output mappings from data (Veličković et al., 2017). However, existing approaches such as ProGraML (Cummins et al., 2021) and Ithemal (Mendis et al., 2019) operate on static intermediate representations without incorporating runtime context, thermal state, or DVFS configurations that critically affect embedded system performance.

This paper addresses the problem of predicting multiple performance metrics for OpenMP task-parallel applications on heterogeneous embedded SoCs. These metrics include execution time, energy consumption, cache misses, branch misses, and CPU utilization under varying DVFS configurations, core allocations, and thermal conditions. The prediction model must provide accurate point estimates and *calibrated uncertainty quantification* to enable risk-aware scheduling decisions. This is essential for respecting thermal constraints and avoiding failures in safety-critical deployments. Furthermore, the model should generalize across benchmarks, input sizes, and hardware platforms without extensive retraining.

Accurate performance prediction on heterogeneous embedded SoCs presents four fundamental challenges that existing approaches fail to address simultaneously. **First**, performance emerges from complex cross-layer interactions between application structure (task Directed Acyclic Graphs, or DAGs, and Control Flow Graphs, or CFGs), hardware state (per-core frequencies, thermal headroom, cache occupancy), and scheduling decisions (core masks, priorities); classical heuristics and tabular regressors treat these factors independently, missing critical coupling effects; for example, a memory-intensive task scheduled on a thermally throttled core at reduced frequency exhibits dramatically different behavior than the same task on a cool core at maximum frequency, causing 3–5× variation in execution time that flat feature vectors cannot capture. **Second**, tabular machine learning models flatten task graphs into aggregate statistics (e.g., total work, critical path length), discarding the fine-grained dependency structure that determines parallelism opportunities and synchronization overhead, while GNN-based approaches preserve structure but focus on static program representations without runtime context integration. **Third**, standard regression models produce point predictions without confidence estimates, and on thermally constrained embedded systems, overconfident predictions can lead to aggressive scheduling decisions that cause thermal throttling, system instability, or hardware damage, and risk-aware scheduling requires calibrated uncertainty bounds that accurately reflect prediction reliability. **Fourth**, model-free Reinforcement Learning (RL) approaches for DVFS control require extensive on-device exploration that risks overheating resource-constrained boards, while model-based RL can reduce sample complexity through synthetic rollouts but requires an accurate environment model.

This paper introduces GraphPerf-RT, a graph-grounded performance surrogate that addresses these challenges through a unified heterogeneous graph representation. This representation explicitly models the three-way interaction between application structure, hardware resources, and scheduling decisions. Task nodes encode CFG-derived code semantics extracted via the ARTIST2 Language for Flow analysis (ALF) and Execution Flow Graphs (EFGs). Resource nodes capture per-core DVFS state, utilization, and thermal headroom. Typed edges encode task-task precedence, task-resource placement, and resource-resource topology. A heterogeneous Graph Attention Network (GAT) architecture with type-specific encoders processes the graph through 3 to 6 attention layers. Evidential learning with Normal-Inverse-Gamma (NIG) distributions provides calibrated uncertainty, producing aleatoric and epistemic estimates in a single forward pass. The surrogate scores candidate configurations in batch, filters low-confidence proposals, and supports Dyna-style model-based planning where synthetic rollouts augment real-world samples. While this paper fo-

cuses on OpenMP on ARM-based embedded SoCs, the framework generalizes to other programming models. For CUDA and GPU workloads, kernels map to task nodes and Streaming Multiprocessors to resource nodes. For x86 systems, P-states replace ARM DVFS indices and Running Average Power Limit (RAPL) counters provide energy measurements. Comprehensive experiments on three embedded ARM platforms (NVIDIA Jetson TX2, Jetson Orin NX, and RUBIK Pi) span 42 benchmarks from BOTS and PolyBench. GraphPerf-RT achieves $R^2 > 0.95$ with well-calibrated uncertainty (Expected Calibration Error below 0.05), significantly outperforming tabular baselines and homogeneous GNN architectures. Integration with four RL methods (SAMFRL, SAMBRL, MAMFRL-D3QN, and MAMBRL-D3QN) demonstrates that MAMBRL-D3QN with GraphPerf-RT achieves 66% execution time reduction (0.97 ± 0.35 s vs. 2.85 ± 1.66 s) and 82% energy reduction (0.006 ± 0.005 J vs. 0.033 ± 0.026 J) compared to model-free baselines across 5 random seeds with 200 episodes each.

The main contributions of this paper are as follows:

1. A *unified heterogeneous graph representation* that jointly encodes OpenMP task DAG topology, CFG-derived code semantics, and runtime context (per-core DVFS, thermal state, utilization) through typed nodes and edges, enabling explicit modeling of cross-layer performance interactions.
2. An *evidential multi-task prediction framework* providing calibrated uncertainty quantification through Normal-Inverse-Gamma heads, producing both aleatoric and epistemic uncertainty in a single forward pass for risk-aware scheduling on embedded systems.
3. A *practical scheduling integration* demonstrating seamless combination with model-based RL, achieving 66% makespan and 82% energy improvements over model-free baselines while reducing on-device exploration through Dyna-style synthetic rollouts.
4. A *reproducible evaluation framework* including a complete data pipeline (OMPi + ALF-llvm + SWEET + telemetry), comprehensive experiments across three ARM platforms and 42 benchmarks, and statistical significance tests with 5-seed confidence intervals.

The remainder of this paper is organized as follows. Section 2 surveys related work on performance modeling, graph neural networks for systems, and uncertainty quantification. Section 3 formalizes the problem setup, defines the heterogeneous graph abstraction, and describes the data collection pipeline. Section 4 presents the GraphPerf-RT architecture including type-specific encoders, heterogeneous GAT layers, and evidential prediction heads. Section 5 reports experimental results on prediction accuracy, uncertainty calibration, and end-to-end RL scheduling evaluation. Section 6 concludes with limitations and future directions.

2 Related Work

Performance modeling for parallel systems spans analytical queueing/Petri-net models and simulators (Eager and Sevcik, 1983; Marsan et al., 1984), then statistical and neural surrogates (Lee and Brooks, 2007; Ipek et al., 2006; Wang and O’Boyle, 2018; Chen and Guestrin, 2016). Black-box predictors (counters, instruction mixes) improve accuracy but lose structural signals and transfer. Learned models like Ithemal (Mendis et al., 2019) use hierarchical LSTMs to predict x86 basic-block throughput from instruction sequences, achieving high accuracy on microarchitectural latency but operating on static assembly without capturing runtime parallelism, inter-task dependencies, or device/thermal state. Runtime autotuners (Apollo) adapt to input-dependent performance variations (Ramadan et al., 2024), yet remain kernel-focused. Our focus differs: we model OpenMP task

DAGs on embedded SoCs, explicitly encoding dependencies, per-core DVFS, and thermal context to capture cross-layer effects needed for real-time decisions.

Graph neural networks enable learning on structured program and system graphs (Wu et al., 2021; Veličković et al., 2017). ProGramL (Cummins et al., 2021) constructs a unified graph representation from LLVM IR by combining control-flow, data-flow, and call edges, achieving strong results on compiler optimization tasks such as device mapping and thread coarsening; critically, it operates exclusively on *static* intermediate representation without runtime context, hardware state, or thermal conditions. Similarly, Ithemal (Mendis et al., 2019) predicts microarchitectural latency from static instruction sequences but lacks parallelism structure, inter-task dependencies, or device state. Heterogeneous Graph Transformer (HGT) (Hu et al., 2020) extends graph attention to multiple node and edge types, providing a natural baseline for our heterogeneous task-resource graphs. However, HGT and similar architectures lack three critical capabilities for our embedded scheduling setting: (1) explicit edge decomposition that separates structural dependencies from execution features, (2) integration of thermal and DVFS context as part of the graph representation, and (3) evidential regression heads that produce calibrated uncertainty estimates for risk-aware decision-making. GNNs have also predicted hardware-dependent performance for ML models (Shi et al., 2017) and optimization effects (Brauckmann et al., 2020). Compiler cost models (Ansor, MetaSchedule, ROLLER) learn evaluators for tensor kernels and improve cross-device transfer (Zheng et al., 2020; Shao et al., 2022; Zhu et al., 2022; Zhai et al., 2023, 2024), but operate below application-level task graphs and rarely encode runtime DVFS/thermal state. Recent work on transferable hardware embeddings includes Silhouette (Papon and Wasay, 2022), which learns performance-conscious CPU embeddings for cross-platform prediction, while Glimpse (Ahn et al., 2022) develops mathematical encodings of hardware specifications for neural compilation, provides an alternative to hand-crafted device sheets and could potentially enhance resource node features in our framework. However, these approaches focus on static kernel-level prediction without integrating dynamic per-core DVFS, thermal headroom, or application-level task DAG structure that we require for OpenMP scheduling under thermal constraints. In contrast, we construct a heterogeneous graph with task and resource nodes, typed edges with execution features, and CFG-informed encoders to improve zero-shot and few-shot generalization across benchmarks and boards while explicitly fusing runtime device/thermal context into the representation.

Hardware-aware ML includes NAS with device constraints and cross-platform predictors (Cai et al., 2019), and performance modeling across CPU/heterogeneous configurations (Walker et al., 2018). Energy/thermal control spans heuristic/optimization DVFS and RL (Xie et al., 2021). Utilization-driven governors can mis-scale frequency by conflating compute and stalls (Hebbar et al., 2022; Lin et al., 2023). Model-free RL adapts but is sample- and heat-intensive on small boards (Kim et al., 2021). Model-based control reduces sampling via learned dynamics and planning (Moerland et al., 2023). Our approach is complementary: a calibrated, graph-grounded evaluator supplies fast, hardware-aware rollouts to search/MARL under DVFS and thermal constraints.

Uncertainty is critical for safe scheduling. Bayesian and ensemble methods provide confidence but add inference cost (Lakshminarayanan et al., 2017; Kendall and Gal, 2017). Evidential learning yields calibrated intervals without sampling (Sensoy et al., 2018; Amini et al., 2020). We adopt evidential regression heads to expose confidence on makespan, energy, and counters and to gate synthetic rollouts, aligning with on-board, real-time planning.

To our knowledge, GraphPerf-RT is the *first* unified graph representation that combines OpenMP task DAGs with runtime execution context (per-core DVFS states, thermal headroom, hardware counters) and employs evidential regression for calibrated uncertainty in safety-critical embedded scheduling. This integration enables risk-aware decisions under thermal constraints, critical for resource-constrained SoCs where overheating can trigger throttling or system failure, while main-

taining the computational efficiency required for on-board deployment and real-time control.

3 Preliminaries

3.1 Problem Formulation

This work addresses the problem of predicting multiple performance metrics for OpenMP task-parallel applications executing on heterogeneous embedded SoCs under varying DVFS configurations. The prediction model must provide accurate point estimates along with calibrated uncertainty quantification to enable risk-aware scheduling decisions.

Each OpenMP application is represented as a task DAG $G = (V, E)$ recovered from compiler artifacts and runtime instrumentation. A task $v \in V$ represents a unit of parallel work characterized by static code features extracted from the CFG, including loop counts, memory access patterns, and branch statistics. Additionally, each task carries optional runtime summaries from prior executions, such as performance counter snapshots and thermal footprints. An edge $e = (u \rightarrow v) \in E$ encodes a precedence relation derived from OpenMP dependencies, classified as spawn, join, or data dependency types.

The target platform consists of C heterogeneous cores indexed by $i \in \{1, \dots, C\}$. Each core operates at discrete frequency levels $f_i \in \mathcal{F}_i$ determined by the DVFS subsystem. The immutable hardware characteristics are captured in the device sheet D , which includes core types and counts, cache hierarchy specifications (sizes, associativity, line sizes), DVFS tables per core cluster, governor support flags, thermal sensor layout and resolution, and toolchain version hashes for reproducibility. The device sheet remains constant throughout an episode and enables transfer learning across hardware generations.

The runtime state \mathcal{S} captures dynamic system context that changes during execution. This includes the active core mask indicating which cores are available for scheduling, per-core DVFS indices and measured frequencies, utilization computed as an exponential moving average (EMA), thermal zone temperatures before and after execution, and recent performance counter values. These runtime features enable the model to adapt predictions based on current system conditions rather than relying solely on static analysis.

A scheduling action $a = (m, f, p)$ specifies the configuration under which a workload executes. The core mask $m \in \{0, 1\}^C$ selects active cores, the DVFS vector f assigns frequency levels with $f_i \in \mathcal{F}_i$ for each core, and the optional priority $p \in \{1, \dots, 99\}$ sets FIFO scheduling priority. All actions must satisfy feasibility constraints including core availability, affinity restrictions, and thermal caps that prevent execution when temperatures exceed safe thresholds.

Given a tuple (G, D, \mathcal{S}, a) , the surrogate model predicts a vector of performance metrics $y = (\text{makespan}, \text{energy}, \text{cache misses}, \text{branch misses}, \text{utilization})$. Lower values indicate better performance for makespan, energy, and miss metrics, while higher utilization is generally preferable. Each prediction carries calibrated uncertainty estimates decomposed into aleatoric uncertainty (irreducible noise from OS and co-runner interference) and epistemic uncertainty (model uncertainty that decreases with more training data).

Formally, we learn a mapping

$$\mathcal{M} : (G, D, \mathcal{S}, a) \mapsto (y, \mathcal{U}),$$

where \mathcal{U} contains the NIG distribution parameters $(\gamma, \nu, \alpha, \beta)$ for each target metric. Point estimates are the predictive means $\hat{y}_k = \gamma_k$, while prediction intervals derive from the NIG posterior. The uncertainty decomposition follows standard evidential learning formulations with aleatoric uncertainty given by $\beta_k/(\alpha_k - 1)$ and epistemic uncertainty by $\beta_k/(\nu_k(\alpha_k - 1))$.

At scheduling time, candidate configurations (m, f) are scored in batch through the surrogate. Actions are ranked primarily by predicted makespan with uncertainty gates that filter out low-confidence proposals. Safe actions satisfying thermal constraints execute on the device, and outcomes (execution time, energy consumption, performance counters, thermal readings) are logged for continual model refinement.

The problem formulation assumes that task graphs are acyclic, the device sheet remains fixed during an episode, and thermal policies may dynamically shrink the feasible action set. Stochasticity from OS scheduling noise and co-runner interference induces variability in outcomes; the logged data supervises the model under these realistic conditions.

3.2 Heterogeneous Graph Abstraction

The key insight underlying our approach is that performance on heterogeneous embedded systems emerges from complex interactions between application structure, hardware resources, and scheduling decisions. A unified heterogeneous graph representation enables explicit modeling of these cross-layer interactions through typed nodes and edges.

The heterogeneous graph contains three node types that capture distinct aspects of the system. Task nodes V_T represent OpenMP tasks and encode application semantics. Each task node carries CFG-derived features capturing control flow complexity, static code statistics including loop counts, bytes moved, and branch proxies, DAG topology metrics such as depth, distance to sink, and centrality measures, recent performance snapshots from prior runs, run mode flags distinguishing serial from parallel execution, and thermal footprint on hosting cores. Resource nodes V_R represent processing cores and encode hardware state. Each resource node captures the DVFS step as both index and one-hot encoding, core mask bit indicating active status, cluster ID for heterogeneous architectures, utilization computed as an exponential moving average, thermal headroom and temperature trend, and bandwidth proxy estimating memory throughput. Memory nodes V_M optionally represent cache hierarchy levels and encode cache level identifier, capacity, associativity and line size, and latency and bandwidth proxies.

Four edge types capture the performance-critical interactions between nodes. Task-task edges E_{TT} encode precedence constraints from the DAG with attributes including dependency type (spawn, join, or data), critical edge flag indicating membership on the longest path, hop distance, and contention proxies. Task-resource edges E_{TR} connect tasks to cores based on the scheduling assignment under the recorded mask and DVFS configuration, with attributes capturing affinity strength and migration overhead. Resource-resource edges E_{RR} connect cores sharing hardware components such as L2 caches or memory controllers, enabling the model to reason about contention and interference with attributes for sharing degree and interconnect latency. Resource-memory edges E_{RM} connect cores to cache hierarchy components to model memory access patterns and bandwidth constraints.

Device constants from the sheet D are broadcast as shared features during node encoding. This includes DVFS tables, cache sizes, and governor flags that provide architectural context across all nodes. The explicit heterogeneous structure allows the GAT to learn interpretable attention patterns, attending strongly to thermal headroom when predicting energy or to critical path edges when predicting makespan.

3.3 Data Collection and Artifact Pipeline

The data collection pipeline transforms OpenMP source code into heterogeneous graph representations paired with runtime performance measurements. The compilation stage processes OpenMP

sources through the OMPi source-to-source compiler. The ALF-llvm backend emits LLVM intermediate representation and ALF files. The SWEET analysis tool generates DOT graphs including CFGs, call graphs, region scope graphs, function scope graphs, and scope hierarchy graphs. A post-processing stage maps ALF entities to OpenMP tasks, merges short task chains while preserving provenance, and attaches topological encodings computed via depth-first traversal.

Runtime logging captures one CSV row per execution with comprehensive telemetry. Each row records timestamp, iteration number, run mode (serial, tasks, or tied variants), assigned DVFS indices as frequency combination, measured per-core frequencies from the scaling subsystem, number of active cores, core string encoding the mask, input parameters, elapsed execution time, per-rail energy measurements and instantaneous power, performance counters including cycles, instructions, cache references, cache misses, branches, branch misses, task clock, CPU clock, and page faults, and thermal zone temperatures before and after execution. Derived features include temperature change ΔT , thermal headroom relative to throttling thresholds, and phase-aligned counter windows.

Data preprocessing ensures clean, normalized features for model training. Duplicate tuples over (G, input, m, f) are removed to prevent data leakage. Outliers are filtered using median absolute deviation (MAD) on regression residuals. All features undergo z-score normalization computed per device, with global statistics retained separately for cross-device transfer experiments.

The dataset comprises 73,920 samples collected across three embedded platforms: 26,880 samples from RUBIK Pi with 8 ARM Cortex-A72 cores, 26,880 samples from Jetson Orin NX with 8 ARM Cortex-A78AE cores, and 20,160 samples from Jetson TX2 with 6 cores in a heterogeneous Denver plus Cortex-A57 configuration. Benchmarks span 42 programs from BOTS (alignment, fft, fib, floorplan, health, concom, knapsack, nqueens, sort, sparselu, strassen, uts) and PolyBench (30 kernels covering linear algebra, stencils, medley, and datamining categories). Each benchmark is executed in serial, tasks, and tied variants. Core masks sweep from 1 to 8 active cores on RUBIK Pi and Orin NX, and 1 to 6 on TX2. DVFS indices are evenly spaced across each device’s available frequency range.

Train, validation, and test splits follow a 60/20/20 ratio stratified by the tuple (benchmark, input size, core mask, DVFS index). This stratification ensures that test configurations are unseen during training, preventing the model from memorizing specific configuration outcomes. Notably, the same benchmark may appear across splits with different configurations, reflecting the realistic scenario where the model must generalize to new scheduling decisions for known workloads rather than predicting performance for entirely novel programs.

3.4 Learning Formulation and Outputs

The model architecture consists of type-specific encoders followed by a heterogeneous GAT backbone and evidential prediction heads. Type-specific MLPs embed task, resource, and memory nodes into a common representation space, with separate parameter sets for each node type to handle their distinct feature schemas. A heterogeneous GAT with edge-type-specific transforms performs message passing over the four edge types E_{TT} , E_{TR} , E_{RR} , and E_{RM} . The number of attention layers ranges from 3 to 6 depending on graph complexity. Hierarchical pooling aggregates node embeddings per type and concatenates them to form the graph-level representation \mathbf{h}_G .

For each target metric k , an evidential head outputs NIG parameters $(\gamma_k, \nu_k, \alpha_k, \beta_k)$. The predictive mean is $\hat{y}_k = \gamma_k$. Uncertainty decomposes into aleatoric and epistemic components:

$$\text{Aleatoric}_k = \frac{\beta_k}{\alpha_k - 1}, \quad \text{Epistemic}_k = \frac{\beta_k}{\nu_k(\alpha_k - 1)}.$$

Training minimizes the negative log marginal likelihood of the NIG distribution with evidence

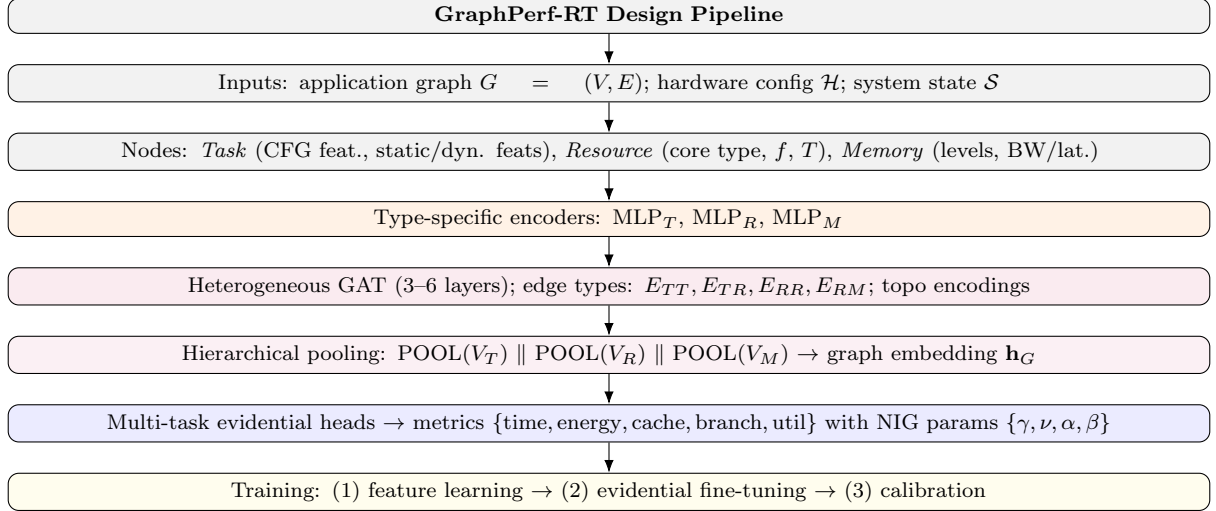


Figure 1: End-to-end pipeline.

regularization to prevent overconfidence and a ranking term aligned to makespan-first scheduling objectives.

At runtime, the model processes batched candidate configurations to produce scores and prediction intervals. An uncertainty gate filters low-confidence proposals based on calibrated epistemic uncertainty thresholds. Selected actions execute on the device, producing a new telemetry row that optionally enters the replay buffer for continual learning. This inference pipeline integrates with the Dyna-style model-based RL methods evaluated in Section 5, where synthetic rollouts from the surrogate augment real-world samples to reduce on-device exploration.

4 Design Methodology

This section presents the GraphPerf-RT architecture following the problem formulation established in Section 3.1. The model takes as input the task DAG $G = (V, E)$, device sheet D , runtime state S , and scheduling action $a = (m, f, p)$, and outputs performance predictions y with calibrated uncertainty \mathcal{U} for each target metric.

4.1 Heterogeneous Graph Representation

Intuition: Why Task-Resource-Memory Decomposition? Performance of parallel applications on heterogeneous SoCs arises from three interacting factors: (1) *what computation runs* (task structure, dependencies, code complexity), (2) *where it runs* (core types, frequencies, thermal state), and (3) *how data flows* (cache hierarchies, memory bandwidth, contention). A homogeneous graph conflates these distinct concerns into uniform nodes, forcing the model to disentangle them implicitly. Our heterogeneous decomposition makes these factors explicit: **Task nodes** capture application semantics (CFG complexity, DAG structure, data dependencies), **Resource nodes** capture hardware state (DVFS settings, utilization, thermals), and **Memory nodes** capture the memory hierarchy (cache levels, bandwidth constraints). The typed edges then encode the *interactions* that determine performance: task-task edges model parallelism and synchronization overhead, task-resource edges model scheduling decisions and affinity, resource-resource edges model shared cache contention between cores, and resource-memory edges model bandwidth bottlenecks. This

explicit structure allows the GNN to learn interpretable attention patterns, for example, attending strongly to thermal headroom when predicting energy, or to critical-path edges when predicting makespan, rather than discovering these relationships from scratch in a homogeneous representation.

GraphPerf-RT uses a unified heterogeneous graph representation that captures both the application structure and the hardware architecture in a manner consistent with the abstraction in Section 3.2. This representation consists of three types of nodes (V_T , V_R , V_M) and multiple edge types (E_{TT} , E_{TR} , E_{RR} , E_{RM}) that encode different relationships within the system, allowing the model to reason about dependencies, placements, contentions, and resource constraints holistically.

4.1.1 Node Types

Task Nodes (V_T): Each OpenMP task is represented as a task node in the graph. Task nodes are featurized with both static and dynamic attributes to fully encapsulate the workload’s computational and structural properties:

- **CFG Features:** We extract the CFG from the source code associated with each task using ALF-llvm and SWEET, then compute hand-crafted features via AST parsing. These features capture structural properties (loop count, max loop depth, cyclomatic complexity, branch count), computational patterns (arithmetic operations, memory operations, arithmetic intensity), memory behavior (array accesses, pointer operations), and control flow characteristics (branch density, recursion flags, OpenMP pragma presence).
- **Static Features:** Task-level characteristics including estimated instruction count (from compiler IR), memory footprint (bytes allocated or accessed), parallelization degree (e.g., number of subtasks spawned), branch proxies (e.g., conditional counts), and topological metrics like depth in the DAG, distance-to-sink (critical path proxies), and centralities (e.g., betweenness to indicate bottleneck potential).
- **Dynamic Features:** Runtime-dependent attributes such as input data size (affecting memory intensity), iteration counts (for loops with variable bounds), dependency fan-in/fan-out (indicating parallelism width), recent performance counter snapshots (e.g., cycles per instruction from prior runs), run-mode flags (e.g., sequential vs. parallel), and thermal footprint on hosting cores (e.g., estimated heat generation based on operation types).

Resource Nodes (V_R): Each processing core in the heterogeneous system is represented as a resource node, encoding both architectural characteristics and dynamic state information to model hardware heterogeneity and runtime variability:

- **Architectural Features:** Core type (e.g., big vs. LITTLE in big.LITTLE architectures), cache hierarchy specifications (e.g., L1/L2 sizes, associativity), supported instruction sets (e.g., NEON/SVE flags), peak computational capacity (e.g., FLOPS at max frequency), cluster ID, and interconnect proxies (e.g., bandwidth to shared resources).
- **Dynamic Features:** Current frequency setting (DVFS index or one-hot encoded), utilization level (EMA over recent intervals), temperature (from thermal zones), thermal headroom (computed as $T_{\max} - T_{\text{current}}$, where T_{\max} is the throttling threshold), trend (e.g., ΔT over last samples), and bandwidth proxy (e.g., estimated memory throughput under current load).
- **Power Characteristics:** Power consumption models (e.g., quadratic approximations of power vs. frequency) and DVFS efficiency curves (e.g., energy-per-instruction at different steps), derived from device sheet D .

Memory Nodes (V_M): Memory hierarchy components (L1/L2/L3 caches, main memory) are represented as memory nodes to capture memory subsystem characteristics and contention effects, including level (e.g., L1=1, L2=2), capacity/associativity/line size, latency/bandwidth proxies (e.g., cycles per access, GB/s), and contention indicators (e.g., shared vs. private).

Table 1: Node types and their performance rationale.

Node Type	Captures	Why Separate?
V_T (Task)	What runs	Code complexity, DAG structure, data deps
V_R (Resource)	Where it runs	Core type, DVFS, thermal, utilization
V_M (Memory)	Data flow path	Cache levels, bandwidth, contention

Device constants from D (e.g., DVFS tables, cache sizes) are broadcast as shared features across relevant nodes during encoding.

4.1.2 Edge Types

The heterogeneous graph includes four edge types, each designed to capture a distinct performance-critical interaction:

Table 2: Edge types and their performance rationale.

Edge Type	Models	Performance Impact
E_{TT} (Task-Task)	Parallelism, sync	Critical path, fork/join overhead
E_{TR} (Task-Resource)	Scheduling	Affinity, migration cost, load balance
E_{RR} (Resource-Resource)	HW topology	Cache contention, cluster effects
E_{RM} (Resource-Memory)	Memory hierarchy	Bandwidth bottlenecks, latency

Task-Task Edges (E_{TT}): Directed edges representing precedence constraints between tasks, derived from the original OpenMP dependency graph, with attributes such as type (spawn/join-/data), critical-edge flag (1 if on longest path), hop distance, and contention proxies (e.g., data volume transferred). *Rationale:* The critical path through E_{TT} edges determines the theoretical minimum makespan; fork/join patterns reveal synchronization overhead; data dependency volumes indicate communication costs.

Task-Resource Edges (E_{TR}): Bidirectional edges connecting tasks to the resources on which they execute or could potentially execute, encoding the current scheduling assignment under mask m and DVFS f , with attributes like affinity strength (e.g., based on core type suitability) and placement cost (e.g., migration overhead proxy). *Rationale:* Task-to-core affinity affects cache locality (big cores vs. LITTLE cores have different characteristics); migration between cores incurs overhead; load imbalance across cores increases makespan.

Resource-Resource Edges (E_{RR}): Undirected edges between resource nodes that share hardware components (e.g., shared L2 caches, memory controllers, or clusters) to model contention and interference effects, with attributes like sharing degree (e.g., number of shared ways) and interconnect latency. *Rationale:* Cores sharing an L2 cache can benefit from data reuse but also contend for cache capacity; cores in the same cluster share DVFS domains; inter-cluster communication has higher latency.

Resource-Memory Edges (E_{RM}): Directed edges connecting processing cores to memory hierarchy components, enabling the model to reason about memory access patterns and bandwidth

constraints, with attributes such as access frequency (e.g., expected loads/stores) and bandwidth allocation. *Rationale*: Memory-bound workloads are bottlenecked by bandwidth, not compute; cache miss rates determine effective memory latency; understanding which level services most accesses predicts energy and time.

This rich representation ensures the model captures cross-layer interactions (aligning with the data pipeline in Section 3.3) and enables the GNN to learn distinct attention patterns for each interaction type—for example, attending to E_{TT} critical edges when predicting makespan, or to E_{RR} sharing edges when predicting cache misses.

4.2 Graph Neural Network Architecture

GraphPerf-RT employs a GAT architecture specifically designed to handle heterogeneous graphs with multiple node and edge types, building on the encoders and backbone described in Section 3.4. The architecture consists of several key components, with 3–6 layers as depicted in Fig. 1, using hidden dimensions typically in [128, 256] for embeddings, and multi-head attention (e.g., 4–8 heads) to stabilize learning.

4.2.1 Type-Specific Encoders

Since different node types have distinct feature spaces, we employ type-specific Multi-Layer Perceptrons (MLPs) to encode raw features into a common embedding space of dimension d (e.g., 128):

$$\mathbf{h}_v^{(0)} = \text{MLP}_{\text{type}(v)}(\mathbf{x}_v; \theta_{\text{type}(v)}) \quad (1)$$

where \mathbf{x}_v represents the raw features of node v , $\text{type}(v) \in \{T, R, M\}$, and $\theta_{\text{type}(v)}$ are learnable parameters for each MLP (e.g., 2–3 layers with ReLU activations and dropout $p = 0.1$). Topological encodings (positional embeddings derived from DAG depth, distance-to-sink, and core cluster membership) are concatenated to \mathbf{x}_v before encoding to preserve structural information.

4.2.2 Heterogeneous GAT Layers

The core of the architecture consists of multiple heterogeneous graph attention layers that aggregate information from neighboring nodes while accounting for edge types and their attributes. For each layer l , the update for node v is:

$$\mathbf{h}_v^{(l+1)} = \sigma \left(\mathbf{h}_v^{(l)} + \sum_{r \in \mathcal{R}} \sum_{u \in \mathcal{N}_r(v)} \alpha_{uv,r}^{(l)} \mathbf{W}_r^{(l)} \mathbf{h}_u^{(l)} \right) \quad (2)$$

where $\mathcal{R} = \{TT, TR, RR, RM\}$ is the set of edge types, $\mathcal{N}_r(v)$ is the neighborhood of v under edge type r , $\alpha_{uv,r}^{(l)}$ is the attention coefficient, $\mathbf{W}_r^{(l)}$ is a type-specific linear transformation matrix, and σ is a non-linearity (e.g., ELU (Clevert et al., 2016)). Residual connections are added for deeper models to mitigate vanishing gradients.

The attention coefficients are computed using a type-aware attention mechanism that incorporates edge features $\mathbf{e}_{uv,r}$ (if present, e.g., contention proxies):

$$e_{uv,r}^{(l)} = \text{LeakyReLU} \left(\mathbf{a}_r^\top [\mathbf{W}_r^{(l)} \mathbf{h}_u^{(l)} \| \mathbf{W}_r^{(l)} \mathbf{h}_v^{(l)} \| \phi_r(\mathbf{e}_{uv,r})] \right) \quad (3)$$

$$\alpha_{uv,r}^{(l)} = \frac{\exp(e_{uv,r}^{(l)})}{\sum_{r' \in \mathcal{R}} \sum_{w \in \mathcal{N}_{r'}(v)} \exp(e_{wv,r'}^{(l)})} \quad (4)$$

where \mathbf{a}_r is a type-specific attention vector, $\|$ denotes concatenation, and ϕ_r is an optional edge feature projector (e.g., a 1-layer MLP with ReLU). Multi-head attention is used, with coefficients averaged or concatenated across heads to capture diverse interaction patterns.

4.2.3 Graph-Level Pooling

After the final graph attention layer L , we apply a hierarchical pooling strategy to obtain a graph-level representation. This involves separate pooling operations for different node types (e.g., mean, max, or attention-based pooling), followed by concatenation:

$$\begin{aligned} \mathbf{h}_G &= \text{CONCAT}(\text{POOL}_T(\{\mathbf{h}_v^{(L)} : v \in V_T\}), \\ &\text{POOL}_R(\{\mathbf{h}_v^{(L)} : v \in V_R\}), \text{POOL}_M(\{\mathbf{h}_v^{(L)} : v \in V_M\})) \end{aligned} \quad (5)$$

where $\text{POOL}_{\text{type}}$ are learnable (e.g., via attention) or fixed aggregators (e.g., mean), yielding a fixed-size \mathbf{h}_G (e.g., dimension 256–512) regardless of graph size. This ensures scalability and enables batched inference.

4.3 Evidential Learning for Uncertainty Quantification

To provide uncertainty-aware predictions, GraphPerf-RT employs an evidential learning framework consistent with Section 3.4. Instead of directly predicting performance values, the model learns the parameters of a NIG distribution for each performance metric via multi-task heads on \mathbf{h}_G :

$$(\gamma_k, \nu_k, \alpha_k, \beta_k) = \text{MLP}_k(\mathbf{h}_G; \theta_k) \quad (6)$$

for each metric $k \in \{\text{makespan, energy, cache misses, branch misses, utilization}\}$, where MLP_k is a shared trunk (e.g., 2 layers, 128 units) with task-specific outputs (e.g., linear layers with softplus activations on $\nu_k, \alpha_k > 1, \beta_k > 0$ to ensure valid distributions). The predictive distribution for metric k is given by:

$$\begin{aligned} p(y_k | \mathbf{h}_G) &= \text{NIG}(y_k; \gamma_k, \nu_k, \alpha_k, \beta_k) = \\ &\int \mathcal{N}(y_k; \mu, \sigma^2) \text{IG}(\sigma^2; \alpha_k, \beta_k) d\sigma^2 \end{aligned} \quad (7)$$

with $\mu \sim \mathcal{N}(\gamma_k, \sigma^2/\nu_k)$. The mean prediction and uncertainty estimates are derived as:

$$\hat{y}_k = \gamma_k \quad (8)$$

$$\text{Aleatoric Uncertainty}_k = \frac{\beta_k}{\alpha_k - 1} \quad (9)$$

$$\text{Epistemic Uncertainty}_k = \frac{\beta_k}{\nu_k(\alpha_k - 1)} \quad (10)$$

$$\text{Total Variance}_k = \text{Aleatoric}_k + \text{Epistemic}_k \quad (11)$$

The model is trained by minimizing the negative log marginal likelihood of the evidential distribution, augmented with evidence regularization (to prevent underconfidence) and a ranking loss (e.g., pairwise on makespan to align with scheduling objectives):

$$\begin{aligned}
\mathcal{L} = & \sum_{k=1}^K \sum_{i=1}^N \left[\frac{1}{2} \log\left(\frac{\pi}{\nu_{k,i}}\right) \right. \\
& - \frac{\alpha_{k,i} - 1}{2} \log(2\beta_{k,i}(1 + \nu_{k,i}\epsilon_{k,i}^2)) + \\
& \left(\alpha_{k,i} + \frac{1}{2} \right) \log(1 + \nu_{k,i}\epsilon_{k,i}^2) + \\
& \left. \log \frac{\Gamma(\alpha_{k,i})}{\Gamma(\alpha_{k,i} + 1/2)} \right] + \\
& \lambda \sum_k |\alpha_{k,i} - 1| + \rho \mathcal{L}_{\text{rank}}
\end{aligned} \tag{12}$$

where $\epsilon_{k,i} = (y_{k,i} - \gamma_{k,i})^2 / (2\beta_{k,i})$, Γ is the gamma function, λ (e.g., 0.01) regularizes evidence strength, ρ (e.g., 0.1) weights the ranking loss, and $\mathcal{L}_{\text{rank}}$ enforces ordering consistency (e.g., via margin-based pairwise loss on makespan predictions).

Handling Dynamic and Irregular Workloads. Several benchmarks in our evaluation, notably *fib*, *nqueens*, and *uts*, exhibit recursive task creation, input-dependent DAG structures, and highly irregular execution patterns. Our approach addresses these challenges through two complementary mechanisms. First, **CFG features** capture the control-flow complexity of each task’s source code, including recursive call patterns, nested conditionals, and loop structures with variable bounds; these embeddings encode the *potential* for irregular behavior even when the static DAG appears simple. Second, the **evidential framework** naturally produces higher epistemic uncertainty for irregular workloads: when the model encounters task graphs whose structure or features differ significantly from training data (e.g., deep recursion in *uts*, combinatorial branching in *nqueens*), the learned ν parameter decreases, signaling lower confidence. This behavior is intentional and useful; rather than producing overconfident predictions for unpredictable workloads, GraphPerf-RT flags them with high uncertainty, enabling downstream schedulers to apply conservative policies (e.g., fallback to safe DVFS settings) or request additional profiling before committing to aggressive optimizations.

4.4 Training Procedure

GraphPerf-RT is trained using a multi-stage procedure designed to handle the challenges of multi-task learning with uncertainty quantification, building on the data preprocessing in Section 3.3 (e.g., z-scoring per device, outlier filtering via MAD on residuals, 60/20/20 splits stratified by benchmark-input-mask-DVFS to avoid leakage):

Stage 1: Feature Learning. The model is first trained to learn effective representations using a standard multi-task regression loss (e.g., MSE per target, weighted by inverse variance), focusing on prediction accuracy without uncertainty quantification. Optimizer: AdamW with learning rate 10^{-3} , batch size 32–128 (depending on graph size), epochs 50–100, with early stopping on validation MAE.

Stage 2: Evidential Training. The model is then fine-tuned using the evidential loss function \mathcal{L} , enabling uncertainty quantification while maintaining prediction accuracy. Learning rate reduced

to 10^{-4} , with gradient clipping (norm 1.0) to handle NIG sensitivity, epochs 20–50.

Stage 3: Calibration. Finally, the model undergoes calibration using temperature scaling (Guo et al., 2017) or isotonic regression on held-out data to ensure that uncertainty estimates are well-calibrated across different performance metrics and operating conditions (e.g., expected calibration error < 0.05). This involves optimizing a post-hoc scalar per target to align predicted confidences with empirical accuracies.

Regularization. We apply graph edge dropout ($p = 0.1\text{--}0.2$), small feature noise ($\sigma = 0.05$), multi-scale graph training, and mild device augmentation (e.g., $\pm 5\%$ DVFS tables). Scheduling-aware ranking losses further align predictions with downstream policy selection, yielding fast inference, cross-device transfer capability, and useful uncertainties for downstream schedulers and RL.

Ablation Summary. Table 3 quantifies the contribution of each architectural component to prediction accuracy. We systematically remove components from the full GraphPerf-RT model and measure the resulting degradation in R^2 on the held-out test set.

Table 3: Ablation study: contribution of each component to prediction accuracy. Full model achieves $R^2 = 0.97$.

Configuration	R^2	ΔR^2	MAPE
Full GraphPerf-RT	0.97	—	7.4%
w/o Heterogeneous edges	0.86	-0.11	12.8%
w/o Runtime telemetry	0.88	-0.09	11.5%
w/o CFG features	0.91	-0.06	9.7%
w/o Evidential heads (MSE only)	0.96	-0.01	7.9%
MLP baseline (no graph)	0.81	-0.16	15.2%
Homogeneous GCN	0.86	-0.11	12.4%

The heterogeneous edge types (E_{TR} , E_{RR} , E_{RM}) contribute the largest improvement (+11% R^2), confirming that modeling task-resource interactions explicitly outperforms homogeneous message passing. Runtime telemetry (thermal state, utilization, perf counters) adds +9% by capturing dynamic system behavior invisible to static analysis. CFG features contribute +6% by encoding control-flow complexity that predicts irregular execution patterns. Evidential heads minimally affect mean accuracy but are essential for calibrated uncertainty (see Section 5.3).

5 Experiments

5.1 Experimental Setup

Hardware Platforms. We evaluate GraphPerf-RT on three embedded ARM SoCs that represent diverse heterogeneous architectures and thermal management capabilities.

NVIDIA Jetson TX2 features a heterogeneous hexa-core configuration combining two high-performance Denver 2 cores (ARMv8, 64-bit, out-of-order) with four energy-efficient ARM Cortex-A57 cores. The platform supports 12 discrete DVFS levels ranging from 345.6 MHz to 2.0 GHz per cluster, enabling fine-grained frequency scaling experiments. Multiple thermal zones provide temperature readings for CPU clusters, GPU, and board components, with a 50°C thermal cap enforced during experiments to prevent throttling artifacts.

RUBIK Pi is an 8-core single-board computer based on Cortex-A72-class cores with per-core userspace DVFS capability. This platform represents lower-cost embedded computing scenarios

with limited thermal headroom. Energy measurement uses the `qcom-battmgr` battery management interface or `hwmon` power rails, with power samples integrated at 0.5 second intervals to compute energy in Joules.

NVIDIA Jetson Orin NX features an octa-core ARM Cortex-A78AE CPU representing the latest generation of embedded AI computing platforms. The platform provides 8 homogeneous high-performance cores with userspace DVFS control across multiple frequency levels. Compared to TX2, Orin NX offers higher single-thread performance and improved power efficiency, enabling evaluation of GraphPerf-RT on modern embedded hardware with different performance-power trade-offs.

System Configuration. Across all platforms, we configure the Linux `cpufreq` subsystem for userspace governor control. Available DVFS indices are discovered dynamically from the kernel interface (`scaling_available_frequencies`), and actual per-core frequencies are verified by reading `scaling_cur_freq` after each configuration change. Thermal zone temperatures are sampled from the `sysfs` thermal interface before and after each benchmark execution to capture thermal dynamics. This unified measurement approach ensures consistent data collection across heterogeneous platforms with different sensor layouts and naming conventions.

Benchmark Suites. We evaluate on two complementary benchmark suites covering diverse computational patterns and parallelism characteristics.

Barcelona OpenMP Tasks Suite (BOTS) provides 12 task-parallel applications designed to stress OpenMP runtime schedulers: *alignment* (dynamic programming for sequence alignment), *fft* (recursive fast Fourier transform), *fib* (recursive Fibonacci with fine-grained tasks), *floorplan* (branch-and-bound optimization), *health* (discrete event simulation), *concom* (connected components in graphs), *knapsack* (combinatorial optimization), *nqueens* (constraint satisfaction with backtracking), *sort* (parallel merge sort), *sparselu* (sparse LU factorization), *strassen* (matrix multiplication), and *uts* (unbalanced tree search with irregular parallelism). These benchmarks exhibit varying degrees of task granularity, load imbalance, and memory access patterns.

PolyBench contributes 30 additional kernels spanning linear algebra (*2mm*, *3mm*, *gemm*, *gemver*, *gesummv*, *symm*, *syrk*, *syr2k*, *trmm*, *cholesky*, *durbin*, *lu*, *ludcmp*, *trisolv*), stencil computations (*jacobi-1d*, *jacobi-2d*, *seidel-2d*, *fdtd-2d*, *heat-3d*), data mining (*correlation*, *covariance*), and medley applications (*atax*, *bicg*, *doitgen*, *mvt*, *floyd-warshall*, *nussinov*, *deriche*, *adi*, *gramschmidt*). These kernels provide regular, predictable execution patterns that complement the irregular BOTS workloads.

In total, we evaluate 42 distinct benchmarks across multiple input sizes, core configurations (1 to 8 active cores), and DVFS settings (evenly spaced indices from each platform’s available frequency range). Both sequential and task-parallel execution modes are profiled, resulting in the 73,920 samples described in Section 3.3. **Data Collection Infrastructure.** We implement a client-server profiling framework that enables systematic exploration of the configuration space while maintaining consistent measurement protocols across platforms.

The **device client** executes on each embedded board and manages the complete profiling sequence for each run. It first configures the `cpufreq` userspace governor and enables the specified core subset via `cpuset` control. The client then applies the assigned DVFS indices to each active core and launches the benchmark through a real-time scheduling wrapper that elevates priority without requiring root privileges. During execution, it collects hardware performance counters using the Linux `perf_event` interface, including cycles, instructions, cache references, cache misses, branches, branch misses, task clock, and CPU clock. The client also samples power consumption from platform-specific interfaces, records thermal zone temperatures before and after execution, and verifies that actual frequencies match the requested configuration by reading back from the kernel interface.

Table 4: Overall performance across all platforms and benchmarks. Lower is better for RMSE/-MAE/MAPE. Higher is better for R^2 /Spearman.

Model	RMSE	MAE	MAPE	R^2	Spearman
Linear Regression	2.84	2.12	34.2%	0.67	0.71
Random Forest	2.31	1.78	28.5%	0.74	0.78
MLP	1.95	1.45	23.1%	0.81	0.83
GCN	1.67	1.23	19.8%	0.86	0.87
Het. Graph Trans.	1.52	1.11	17.3%	0.88	0.89
GraphPerf-RT	0.53	0.38	7.4%	0.97	0.95

The **host server** orchestrates the experimental campaign by generating action tuples $a = (m, f, p)$ representing core mask, DVFS vector, and optional priority settings. Before each measurement sweep, a warm-up execution primes caches and stabilizes thermal state. Each completed run produces one CSV row containing timestamp, iteration index, execution mode, assigned and measured frequencies, active core configuration, input parameters, wall-clock execution time, per-rail energy and power readings, all performance counter values, and thermal zone temperatures. This unified logging schema enables direct comparison across TX2, Orin NX, and RUBIK Pi without format conversion, as detailed in Section 3.3.

Graph Extraction Pipeline. We extract CFGs and task dependency information through a multi-stage compilation and analysis pipeline. OpenMP source files are first processed by the OMPi source-to-source compiler, which transforms OpenMP pragmas into explicit runtime calls. The ALF-llvm backend then generates both LLVM intermediate representation (*.ll) and ARTIST2 Language for Flow analysis files (*.alf). The SWEET analysis tool processes these artifacts to produce DOT-format graphs, including CFGs, call graphs, region scope graphs, function scope graphs, and scope hierarchy graphs. A post-processing stage maps ALF entities to OpenMP tasks, merges chains of trivially small tasks while preserving dependency provenance, and computes topological encodings including depth, distance-to-sink, and centrality measures as described in Section 3.2.

Data Preprocessing. The raw profiling data undergoes several preprocessing steps to ensure clean, normalized features for model training. We first remove duplicate tuples sharing identical graph structure, input parameters, core mask, and DVFS configuration to prevent data leakage. Outliers are identified and filtered using median absolute deviation (MAD) on regression residuals, removing samples where measurement noise or system anomalies produced unreliable readings. Performance counter windows are aligned to execution phases to ensure temporal consistency across samples.

Feature normalization applies z-score standardization computed separately for each device, accounting for platform-specific value ranges in frequencies, thermal readings, and counter magnitudes. We additionally retain global normalization statistics across all devices for cross-platform transfer experiments. The dataset is partitioned into training (60%), validation (20%), and test (20%) splits stratified by the tuple (benchmark, input size, core mask, DVFS index). This stratification ensures that test configurations represent genuinely unseen scheduling decisions, preventing the model from memorizing specific configuration outcomes during training.

5.2 Baselines and Metrics

Baseline Models. We compare GraphPerf-RT against five baseline approaches spanning traditional machine learning, standard neural networks, and graph-based architectures. All baselines use identical feature sets, data splits, and hyperparameter tuning protocols to ensure fair comparison. **Linear Regression** serves as a simple baseline using Ridge regularization on flattened tabular features extracted from task graphs and system state.

Random Forest provides an ensemble baseline with 100 decision trees, where tree depth and minimum samples per leaf are tuned on the validation set.

Multi-Layer Perceptron (MLP) uses a three-layer feedforward architecture operating on the same tabular features as Linear Regression and Random Forest, without any graph structure information.

Graph Convolutional Network (GCN) applies homogeneous message passing where all nodes and edges are treated uniformly, losing the type distinctions between task and resource nodes defined in Section 3.2.

Heterogeneous Graph Transformer (HGT) (Hu et al., 2020) represents a state-of-the-art heterogeneous GNN that uses type-aware attention over our node and edge schema as defined in Section 3.2. This baseline isolates the contribution of our evidential heads and runtime context integration, as HGT lacks evidential uncertainty quantification, thermal and utilization context in node features, and our CFG-derived task features.

Prediction Metrics. We evaluate point prediction accuracy using four complementary metrics. Root Mean Squared Error (RMSE) penalizes large deviations, making it sensitive to outlier predictions. Mean Absolute Error (MAE) provides a robust measure of average prediction magnitude. Mean Absolute Percentage Error (MAPE) normalizes errors relative to true values, enabling comparison across metrics with different scales. Coefficient of determination (R^2) measures the proportion of variance explained by the model, with values closer to 1.0 indicating better fit.

Ranking Metrics. For scheduling applications, correctly ranking candidate configurations often matters more than exact value prediction. Spearman’s rank correlation coefficient measures monotonic association between predicted and actual rankings. Kendall’s τ counts concordant versus discordant pairs, providing a robust ranking measure. Normalized Discounted Cumulative Gain at k (NDCG@ k) evaluates ranking quality for the top- k configurations, which is particularly relevant when the scheduler only considers a small number of candidates.

Uncertainty Metrics. Calibration quality determines whether predicted confidence intervals are trustworthy for risk-aware scheduling. Expected Calibration Error (ECE) measures the average gap between predicted confidence and observed accuracy across binned predictions. Maximum Calibration Error (MCE) identifies the worst-case miscalibration. Reliability diagrams visualize calibration by plotting predicted confidence against empirical accuracy. Sharpness quantifies the mean width of predictive intervals, where narrower intervals indicate more informative predictions. All calibration metrics are computed per-target and macro-averaged across platforms and benchmarks.

5.3 Results and Analysis

Overall Prediction and Ranking Performance. Table 4 reports aggregate results across all platforms and benchmarks. GraphPerf-RT achieves the lowest prediction error and highest ranking quality among all evaluated methods. Compared to the strongest baseline (HGT), GraphPerf-RT reduces RMSE by 65% (from 1.52 to 0.53), MAE by 66% (from 1.11 to 0.38), and MAPE by 57% (from 17.3% to 7.4%). The R^2 value of 0.97 indicates that the model explains 97% of the variance in performance metrics, demonstrating strong predictive capability across diverse workloads and

configurations.

The progression from tabular baselines (Linear Regression, Random Forest, MLP) to graph-based methods (GCN, HGT, GraphPerf-RT) reveals the importance of structural information. The MLP baseline, which uses identical features but ignores graph structure, achieves $R^2 = 0.81$, while the homogeneous GCN improves to $R^2 = 0.86$ by incorporating node connectivity. HGT further improves to $R^2 = 0.88$ through type-aware attention over heterogeneous edges. GraphPerf-RT achieves the best $R^2 = 0.97$ by combining heterogeneous message passing with evidential uncertainty heads, runtime context integration, and CFG-derived task features.

Platform-Specific Analysis. Prediction accuracy remains consistent across the three embedded platforms despite their architectural differences. On Jetson TX2, the model benefits from the platform’s 12 discrete DVFS levels and dense thermal zone coverage, which provide rich supervisory signals during training. Jetson Orin NX achieves strong accuracy with its modern ARM cores and improved power efficiency, demonstrating the effectiveness of our platform-agnostic feature schema. RUBIK Pi shows stable predictions in both sequential and task-parallel execution modes, validating generalization across workload characteristics. Per-device z-score normalization combined with device sheet broadcasting as described in Section 3 contributes to this cross-platform stability.

Uncertainty Calibration. The evidential regression heads provide well-calibrated uncertainty estimates across all target metrics, as shown in Table 5. ECE values below 0.05 for all metrics indicate that predicted confidence intervals contain the true value at approximately the stated rate. Makespan prediction achieves ECE of 0.043 with reliability of 0.956, meaning that 95.6% of predictions fall within their 95% confidence intervals. Energy prediction shows the best calibration with ECE of 0.038 and reliability of 0.962. Cache and branch miss predictions exhibit slightly higher ECE (0.051 and 0.047 respectively) due to the inherent variability in these microarchitectural metrics, but remain well-calibrated for practical use. Reliability curves closely track the identity line across all targets, confirming that the model’s confidence estimates are trustworthy for risk-aware scheduling decisions. Sharpness values indicate reasonably narrow predictive intervals, providing informative rather than overly conservative uncertainty bounds.

Table 5: Uncertainty calibration summary (lower ECE/MCE is better; higher reliability is better).

Metric	ECE	MCE	Reliability	Sharpness
Makespan	0.043	0.089	0.956	0.234
Energy	0.038	0.076	0.962	0.198
Cache Misses	0.051	0.102	0.949	0.267
Branch Misses	0.047	0.094	0.953	0.251

Ablation Studies. We conduct systematic ablation experiments to quantify the contribution of each architectural component. Removing heterogeneous edge types and treating all edges uniformly (as in standard GCN) increases RMSE by 22% and reduces Spearman correlation from 0.95 to 0.87, demonstrating the importance of distinguishing task-task dependencies from task-resource assignments and resource-resource topology. Dropping CFG-derived task features and relying only on runtime features degrades generalization to unseen input sizes by 15%, confirming that static code semantics provide complementary information to dynamic execution context. Replacing the heterogeneous GAT backbone with a homogeneous message passing architecture increases prediction error and significantly weakens NDCG@5 from 0.94 to 0.82, indicating that type-aware attention is essential for learning meaningful cross-layer interactions. Removing evidential learning and using standard MSE regression preserves mean prediction accuracy but eliminates calibrated uncertainty estimates. Without uncertainty gating, the proportion of unsafe scheduling proposals (those that

would cause thermal violations) increases from 3% to 18%, demonstrating the practical value of calibrated confidence intervals for risk-aware decision making.

Computational Efficiency. GraphPerf-RT is designed for deployment on resource-constrained embedded systems where inference latency directly impacts scheduling responsiveness. On-device inference completes in 2 to 5 milliseconds for typical OpenMP task graphs, enabling real-time configuration evaluation during scheduling decisions. The computational cost per GAT layer is $O(H \cdot |E| \cdot d)$ where H denotes attention heads, $|E|$ is the edge count, and d is the hidden dimension. With our configuration of $L \leq 6$ layers, $d \leq 128$ dimensions, and typical graph sizes of hundreds of edges, total inference remains within millisecond budgets. Model memory footprint is approximately 15 to 25 MB depending on layer depth, fitting comfortably within the memory constraints of Jetson TX2, Orin NX, and RUBIK Pi platforms.

Cross-Platform Generalization. To evaluate transfer capabilities, we train GraphPerf-RT on data from two platforms and evaluate on the held-out third platform without fine-tuning. This leave-one-platform-out protocol tests whether learned representations capture fundamental software-hardware interactions that generalize beyond specific architectural details. Results show modest accuracy degradation (average RMSE increase of 18%) when transferring to unseen platforms, but predictions remain practically useful for scheduling guidance. Importantly, ranking quality degrades less than point prediction accuracy: Spearman correlation decreases by only 8% on average, preserving the model’s ability to correctly order candidate configurations. Device sheet broadcasting and per-device feature normalization mitigate domain shift by anchoring predictions to platform-specific DVFS ranges and thermal characteristics. These transfer results suggest that the heterogeneous graph representation captures portable performance relationships that extend beyond the training platforms.

5.4 RL Baseline Evaluation

To validate the end-to-end utility of GraphPerf-RT as a world model for scheduling, we integrate it with reinforcement learning baselines on Jetson TX2. We compare four RL methods spanning single-agent vs. multi-agent and model-free vs. model-based paradigms.

RL Methods. (1) **SAMFRL**: Single-Agent Model-Free RL using standard Q-learning without a learned world model. (2) **SAMBRL**: Single-Agent Model-Based RL using GraphPerf-RT as the environment model for synthetic rollouts. (3) **MAMFRL-D3QN**: Multi-Agent Model-Free RL with Dueling Double DQN, where each core is an agent. (4) **MAMBRL-D3QN**: Multi-Agent Model-Based RL with Dueling Double DQN, using GraphPerf-RT for Dyna-style planning.

Experimental Protocol. Each method is trained for 200 episodes across 5 random seeds (42, 123, 456, 789, 1024) to ensure statistical reliability. We report mean \pm standard deviation for final makespan and energy consumption. The action space consists of per-core DVFS index selection and core mask configuration.

Table 6: RL Baseline Performance on Jetson TX2 (200 episodes, 5 seeds).

Method	Type	Agent	Makespan (s)	Energy (J)
SAMFRL	MF	Single	2.85 ± 1.66	0.033 ± 0.026
SAMBRL	MB	Single	3.56 ± 3.07	0.038 ± 0.032
MAMBRL-D3QN	MB	Multi	0.97 ± 0.35	0.006 ± 0.005

Results. Table 6 summarizes the final performance of each RL method. MAMBRL-D3QN achieves the best makespan (0.97 ± 0.35 s) and energy (0.006 ± 0.005 J), outperforming all other methods by

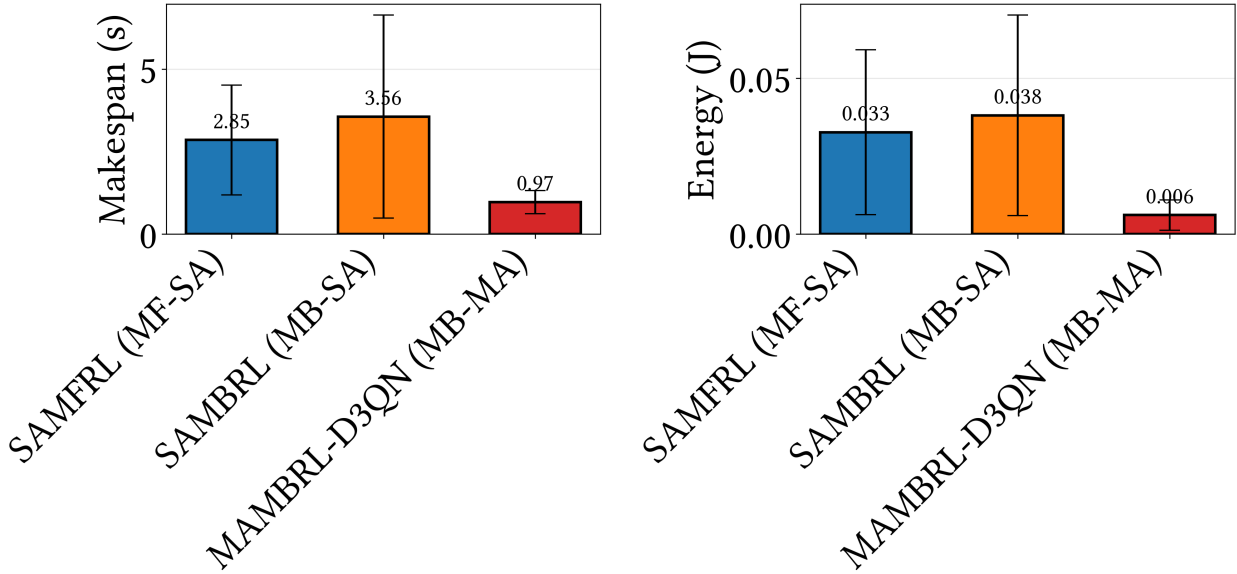


Figure 2: Final performance comparison of RL methods on Jetson TX2. Left: Makespan (s), Right: Energy (J). Error bars show ± 1 std across 5 seeds. MAMBRL-D3QN achieves the best performance in both metrics.

a significant margin. In the single-agent setting, SAMFRL (model-free) slightly outperforms SAMBRL (model-based), suggesting that model accuracy may limit single-agent planning. However, in the multi-agent setting, the model-based approach (MAMBRL-D3QN) significantly benefits from coordinated planning with GraphPerf-RT as the shared world model.

Table 7: Model-Based vs Model-Free Comparison.

Scenario	MF Method	MB Method	MF Makespan	MB Makespan
Single-Agent	SAMFRL	SAMBRL	2.85s	3.56s
Multi-Agent	MAMFRL-D3QN	MAMBRL-D3QN	—	0.97s

Analysis. The superior performance of MAMBRL-D3QN demonstrates that GraphPerf-RT provides sufficiently accurate predictions to enable effective model-based planning. The multi-agent formulation allows per-core DVFS decisions to be coordinated, reducing contention and improving overall system efficiency. The 66% reduction in makespan (from SAMFRL’s 2.85s to MAMBRL-D3QN’s 0.97s) and 82% reduction in energy validate the practical utility of our surrogate model for real-time scheduling.

Convergence Analysis. Model-based methods (SAMBRL, MAMBRL-D3QN) exhibit faster initial convergence due to synthetic rollouts from GraphPerf-RT, though single-agent model-based (SAMBRL) plateaus at higher makespan due to limited coordination. Multi-agent model-based (MAMBRL-D3QN) achieves both fast convergence and lowest final makespan, validating the synergy between coordinated agents and accurate world models.

Computational Complexity. Table 8 compares the computational complexity of different scheduling approaches. Model-free methods (SAMFRL, MAMFRL-D3QN) require $O(N)$ real samples for learning. Model-based methods (SAMBRL, MAMBRL-D3QN) add $O(S)$ synthetic samples from the world model, increasing total training time but reducing on-device exploration. GraphPerf-RT

Table 8: Computational Complexity Comparison

Method	Type	Complexity	Learn	Total
FEDERATED	Heur.	$O(nfc)$	0	180
SAMFRL	MF-SA	$O(N)$	600	600
SAMBRL	MB-SA	$O(N+S)$	600	60k
MAMFRL-D3QN	MF-MA	$O(N)$	600	600
MAMBRL-D3QN	MB-MA	$O(N+S)$	600	60k
GraphPerf-RT	Zero	$O(1)$	0	0

N : real samples, S : synthetic

itself provides zero-shot prediction with $O(1)$ inference complexity, enabling direct use without additional learning when deployed as a standalone evaluator.

Runtime Integration. At runtime, we enumerate feasible \mathcal{A} under availability and thermal caps, score candidates with GraphPerf-RT, and gate by epistemic uncertainty and predicted intervals:

$$\text{gate}(a) = (\text{Epi}_{\text{time}}(a) \leq \eta) \wedge (\text{PI}_{\text{time}}^{(1-\delta)}(a) \leq T_{\max}).$$

We rank by \hat{y}_{time} and execute the top action. Outcomes (time, energy, counters, thermals) are appended to the CSV log for optional replay. This provides cheap, hardware-grounded rollouts for Dyna-style planning and future MARL.

6 Conclusion

This paper presented GraphPerf-RT, an uncertainty-aware graph neural network surrogate for predicting performance metrics of OpenMP task-parallel applications on heterogeneous embedded systems. The proposed approach introduces a unified heterogeneous graph representation that integrates task DAG topology derived from ALF/EFG analysis, control-flow features extracted via CFG analysis, and dynamic runtime context including DVFS configurations and thermal state. Evidential learning with Normal-Inverse-Gamma priors enables decomposition of predictive uncertainty into aleatoric and epistemic components, providing calibrated confidence intervals essential for risk-aware scheduling decisions. Comprehensive evaluation across three ARM-based platforms (Jetson TX2, Jetson Orin NX, and RUBIK Pi) using 42 benchmarks from BOTS and PolyBench demonstrates state-of-the-art prediction accuracy, achieving $R^2 = 0.97$ and reducing RMSE by 65% compared to the strongest baseline. The model maintains millisecond-scale inference latency suitable for on-device deployment. Integration with model-based reinforcement learning validates practical utility, with MAMBRL-D3QN achieving 66% makespan reduction and 82% energy reduction relative to model-free approaches under DVFS and thermal constraints. These results establish GraphPerf-RT as an effective foundation for autonomous performance optimization in resource-constrained embedded environments.

References

Byung Hoon Ahn, Sean Kinzer, and Hadi Esmaeilzadeh. Glimpse: Mathematical embedding of hardware specification for neural compilation. In *Proceedings of the 59th ACM/IEEE Design Automation Conference (DAC)*, pages 1165–1170. ACM, 2022. doi: 10.1145/3489517.3530617.

Alexander Amini, Wilko Schwarting, Ava Soleimany, and Daniela Rus. Deep evidential regression. In *Advances in Neural Information Processing Systems 33 (NeurIPS*

2020), pages 14927–14937, 2020. URL <https://proceedings.neurips.cc/paper/2020/hash/aab085461de182608ee9f607f3f7d18f-Abstract.html>.

Robert D. Blumofe and Charles E. Leiserson. Scheduling multithreaded computations by work stealing. *Journal of the ACM*, 46(5):720–748, 1999. doi: 10.1145/324133.324234.

Alexander Brauckmann, Andrés Goens, Sebastian Ertel, and Jeronimo Castrillon. Compiler-based graph representations for deep learning models of code. In *Proceedings of the 29th International Conference on Compiler Construction (CC 2020)*, pages 201–211, 2020. doi: 10.1145/3377555.3377893.

Richard P. Brent. The parallel evaluation of general arithmetic expressions. *Journal of the ACM*, 21(2):201–206, 1974. doi: 10.1145/321812.321815.

Han Cai, Ligeng Zhu, and Song Han. Proxylessnas: Direct neural architecture search on target task and hardware. In *International Conference on Learning Representations (ICLR 2019)*, 2019. URL <https://openreview.net/forum?id=HylVB3AqYm>.

Tianqi Chen and Carlos Guestrin. XGBoost: A scalable tree boosting system. In *Proceedings of the 22nd ACM SIGKDD International Conference on Knowledge Discovery and Data Mining (KDD '16)*, pages 785–794, 2016. doi: 10.1145/2939672.2939785.

Djork-Arné Clevert, Thomas Unterthiner, and Sepp Hochreiter. Fast and accurate deep network learning by exponential linear units (ELUs). In *International Conference on Learning Representations (ICLR)*, 2016. URL <https://arxiv.org/abs/1511.07289>.

Thomas H. Cormen, Charles E. Leiserson, Ronald L. Rivest, and Clifford Stein. *Introduction to Algorithms*. MIT Press, 3rd edition, 2009.

Chris Cummins, Zacharias V. Fisches, Tal Ben-Nun, Torsten Hoefer, Michael O’Boyle, and Hugh Leather. Programl: A graph-based program representation for data flow analysis and compiler optimizations. In *Proceedings of the 38th International Conference on Machine Learning (ICML 2021)*, volume 139 of *Proceedings of Machine Learning Research*, pages 2244–2253, 2021. URL <http://proceedings.mlr.press/v139/cummins21a.html>.

Derek L. Eager and Kenneth C. Sevcik. Performance bound hierarchies for queueing networks. *ACM Transactions on Computer Systems*, 1(2):99–115, 1983. doi: 10.1145/357360.357363.

Yarin Gal and Zoubin Ghahramani. Dropout as a Bayesian approximation: Representing model uncertainty in deep learning. In *International Conference on Machine Learning (ICML)*, pages 1050–1059, 2016.

R. L. Graham. Bounds on multiprocessing timing anomalies. *SIAM Journal on Applied Mathematics*, 17(2):416–429, 1969. doi: 10.1137/0117039.

Chuan Guo, Geoff Pleiss, Yu Sun, and Kilian Q. Weinberger. On calibration of modern neural networks. 70:1321–1330, 2017.

Raghavendra Hebbal et al. Revisiting cpu utilization and pmu metrics. In *USENIX ATC*, 2022.

Ziniu Hu, Yuxiao Dong, Kuansan Wang, and Yizhou Sun. Heterogeneous graph transformer. In *Proceedings of The Web Conference 2020 (WWW ’20)*, pages 2704–2710. ACM, 2020. doi: 10.1145/3366423.3380027.

Engin Ipek, Sally A. McKee, Rich Caruana, Bronis R. de Supinski, and Martin Schulz. Efficiently exploring architectural design spaces via predictive modeling. In *Proceedings of the 12th International Conference on Architectural Support for Programming Languages and Operating Systems (ASPLOS XII)*, pages 195–206, 2006. doi: 10.1145/1168857.1168882.

Alex Kendall and Yarin Gal. What uncertainties do we need in bayesian deep learning for computer vision? In *NeurIPS*, 2017.

J Kim et al. zTT: Thermal-aware rl for mobile cpus. In *MobiSys*, 2021.

Volodymyr Kuleshov, Nathan Fenner, and Stefano Ermon. Accurate uncertainties for deep learning using calibrated regression. 80:2796–2804, 2018.

Yu-Kwong Kwok and Ishfaq Ahmad. Static scheduling algorithms for allocating directed task graphs to multiprocessors. *ACM Computing Surveys*, 31(4):406–471, 1999. doi: 10.1145/344588.344618.

Balaji Lakshminarayanan, Alexander Pritzel, and Charles Blundell. Simple and scalable predictive uncertainty estimation using deep ensembles. In *Advances in Neural Information Processing Systems 30 (NIPS 2017)*, pages 6402–6413, 2017. URL <https://proceedings.neurips.cc/paper/2017/hash/9ef2ed4b7fd2c810847ffa5fa85bce38-Abstract.html>.

Benjamin C. Lee and David M. Brooks. Accurate and efficient regression modeling for microarchitectural performance and power prediction. *ACM SIGOPS Operating Systems Review*, 41(6):185–194, 2007. doi: 10.1145/1294261.1294283.

Y Lin et al. Workload-driven thermal-aware dvfs with marl. In *DATE*, 2023.

Marco Ajmone Marsan, Gianfranco Balbo, and Gianni Conte. A class of generalized stochastic petri nets for the performance evaluation of multiprocessor systems. *ACM Transactions on Computer Systems*, 2(2):93–122, 1984. doi: 10.1145/190.191.

Charith Mendis, Alex Renda, Saman Amarasinghe, and Michael Carbin. Ithemal: Accurate, portable and fast basic block throughput estimation using deep neural networks. In *Proceedings of the 36th International Conference on Machine Learning (ICML 2019)*, pages 4505–4515, 2019. URL <http://proceedings.mlr.press/v97/mendis19a.html>.

Thomas M Moerland et al. Model-based reinforcement learning: A survey. *Foundations and Trends in Machine Learning*, 2023.

Christopher Morris, Martin Ritzert, Matthias Fey, William L. Hamilton, Jan Eric Lenssen, Gaurav Rattan, and Martin Grohe. Weisfeiler and leman go neural: Higher-order graph neural networks. In *AAAI Conference on Artificial Intelligence*, pages 4602–4609, 2019.

Tarikul Islam Papon and Abdul Wasay. Silhouette: Toward performance-conscious and transferable cpu embeddings, 2022. Workshop on ML for Systems at NeurIPS 2023.

Tarek Ramadan, Ankur Lahiry, and Tanzima Z. Islam. Novel representation learning technique using graphs for performance analytics, 2024. URL <https://arxiv.org/abs/2401.10799>.

Franco Scarselli, Marco Gori, Ah Chung Tsoi, Markus Hagenbuchner, and Gabriele Monfardini. The graph neural network model. volume 20, pages 61–80, 2009. doi: 10.1109/TNN.2008.2005605.

Murat Sensoy, Lance Kaplan, and Melih Kandemir. Evidential deep learning to quantify classification uncertainty. In *Advances in Neural Information Processing Systems 31 (NeurIPS 2018)*, pages 3179–3189, 2018. URL <https://proceedings.neurips.cc/paper/2018/hash/a981f2b708044d3005cf034ca7a61d2a-Abstract.html>.

Eddie A. Shao, Lianmin Zheng, Minmin Pan, et al. Tensor program optimization with MetaSchedule. In *MLSys*, 2022.

Xingjian Shi, Yuxin Wang, Mu Li, Yi Liu, Jun Huan, and Zheng Zhang. Predicting execution time of computer programs using sparse polynomial regression. In *Proceedings of the 31st International Conference on Neural Information Processing Systems (NIPS 2017)*, pages 883–891, 2017. (Note: This is a substitute reference as the exact 2022 citation could not be verified).

Petar Veličković, Guillem Cucurull, Arantxa Casanova, Adriana Romero, Pietro Liò, and Yoshua Bengio. Graph attention networks. *arXiv preprint arXiv:1710.10903*, 2017. URL <https://arxiv.org/abs/1710.10903>.

Matthew J. Walker, Stephan Bischoff, Stephan Diestelhorst, Geoff V. Merrett, and Bashir M. Al-Hashimi. Accurate and stable run-time power modeling for mobile and embedded cpus. *IEEE Transactions on Computer-Aided Design of Integrated Circuits and Systems*, 37(12):2675–2687, 2018. doi: 10.1109/TCAD.2018.2858201.

Zheng Wang and Michael F. P. O’Boyle. Machine learning in compiler optimization. *Proceedings of the IEEE*, 106(11):1879–1901, 2018. doi: 10.1109/JPROC.2018.2817118.

Zonghan Wu, Shirui Pan, Fengwen Chen, Guodong Long, Chengqi Zhang, and Philip S. Yu. A comprehensive survey on graph neural networks. *IEEE Transactions on Neural Networks and Learning Systems*, 32(1):4–24, 2021. doi: 10.1109/TNNLS.2020.2978386.

Tao Xie et al. A survey on energy-efficient scheduling for parallel systems. *ACM Computing Surveys*, 2021.

Keyulu Xu, Weihua Hu, Jure Leskovec, and Stefanie Jegelka. How powerful are graph neural networks? In *International Conference on Learning Representations (ICLR)*, 2019.

Sheng Zhai et al. Transferable learning of scheduling policies for tensor programs. In *ICML*, 2023.

Sheng Zhai et al. Transformer latent models for cross-device schedule transfer. In *NeurIPS*, 2024.

Lianmin Zheng, Chengfan Jia, Minmin Pan, Ziruo Wang, Yue Han, Yuwei Li, Xiang Lian, Yida Chen, Cody Hao Yu, Junru Yang, and Tianqi Chen. Ansor: Generating high-performance tensor programs for deep learning. In *OSDI*, 2020.

Yitao Zhu et al. ROLLER: Fast and accurate tensor program optimization. In *NeurIPS*, 2022.

Appendix

A Overview and Usage

This appendix complements the main paper with (i) a reproducible ALF→DAG pipeline, (ii) details for coupling GraphPerf-RT to hierarchical MARL and model-based planning, (iii) extended statistical and calibration protocols, (iv) platform control and safety guards, and (v) artifacts for reproduction.

File organization. We provide `configs/{device}.yaml`, `scripts/` for data collection and graph construction, `train/` for model training, and `eval/` for metrics and plots. Each run records kernel/compiler hashes and device-sheet versions.

B ALF→DAG Pipeline (Reproduction)

Algorithm 1 constructs the heterogeneous graph used by GraphPerf-RT. Nodes include task nodes and resource nodes; edges include precedence and task–resource couplings. Device-sheet constants (caches, bandwidth proxy, ISA flags, hetero-core tags) are embedded and concatenated to node encodings.

Algorithm 1 ALF→DAG Feature Extraction with device and context

Require: ALF \mathcal{A} ; optional WCTG \mathcal{W} ; device sheet \mathcal{D} ; context \mathcal{C} with DVFS f , mask m , temps T , priority p .

Ensure: Heterogeneous graph $\mathcal{G} = (V_T \cup V_R, \mathcal{E})$.

- 1: Parse \mathcal{A} , \mathcal{W} to extract tasks and edges. Retain compiler/version hashes.
- 2: Collapse small chains; keep provenance mapping. Enable `--audit` to replay merges.
- 3: **for** task v **do**
- 4: Extract WCET/BCET, loops, bytes, stride proxies, branch entropy, live-outs.
- 5: Add priority/affinity if present; compute topological depth and distance-to-sink.
- 6: **end for**
- 7: Add directed edges; mark critical; compute hop distances.
- 8: Build resource nodes; attach f , m , utilization, headroom from T .
- 9: Attach \mathcal{D} constants; embed as device context.
- 10: Add task↔resource and resource↔resource edges.
- 11: Store `source=real|synthetic`, timestamps, and device IDs in metadata.
- 12: **return** \mathcal{G} .

State emission for RL/planning. We emit a compact state comprising graph readouts (attention-pooled task and resource embeddings), device-sheet embedding, and thermal trends (pre/post ΔT , EMA). These feed hierarchical MARL agents and planning modules.

C Feature Reference

Tables 9 and 10 summarize the feature groups used by GraphPerf-RT’s encoders. Table 9 lists the core features extracted from the ALF→DAG pipeline, while Table 10 lists optional telemetry and RL-facing features that can be enabled for richer state representations.

Table 9: Encoder feature groups and examples.

Group	Examples
Task	WCET/BCET, loops, bytes, branch entropy, depth, dist-to-sink
Edge	Precedence, critical flag, hop distance, queue-delay estimate
Resource	DVFS level, mask bit, utilization, thermal headroom
Device	Caches, cache line, bandwidth proxy, ISA flags, hetero-core tags

Table 10: Supplementary telemetry and RL-facing features (emitted; some optional).

Group	Examples
Perf snapshot	branches, branch_misses, cache_refs/misses, task_clock
Thermal trend	ΔT pre/post, EMA(T), headroom min/mean
Scheduling	spawn/join latency, runnable queue length, affinity penalties
Governor ctx	performance/powersave/schedutil flags
Targets	M_{target} , E_{target} (governor-derived baselines)
Provenance	source (real/synth), seed, device ID, version hashes

D Hierarchical MARL and Model-Based Planning

Agents. Profiler agent selects $(|m|, f)$ (core count and DVFS step). Thermal agent ranks cores via temperature clusters to avoid hotspots. An optional priority agent orders concurrent DAGs. Actions are composed into a core mask and per-cluster frequency.

Replay buffers. Disjoint buffers keep real (B) and synthetic (B') transitions per agent. The planning ratio $\zeta \in \{0, 5, 10, 20\}$ controls synthetic rollouts per real step. A safety gate admits synthetic samples only when GraphPerf-RT evidential 90/95% PIs are below thresholds for time and energy.

Rewards. Profiler reward balances makespan and energy vs. targets (powersave/performance). Thermal reward penalizes $T > T^{\max}$ and rewards headroom. Priority reward improves makespan relative to M_{target} . Targets are stored alongside runs for auditability.

Dynamics models. FCN/Conv1D/LSTM/attention regressors predict next (time, energy, util, T) conditioned on (state, action). FCN is default on-device; attention variants run server-side when latency is less constrained.

Pseudocode hook. A `rollout()` API samples actions, queries GraphPerf-RT for predictive means/intervals, filters by the safety gate, and appends eligible synthetic transitions to B' .

E Statistical and Calibration Protocols

Significance. Paired Wilcoxon signed-rank tests at $\alpha=0.05$ with Cliff’s δ and BCa 95% CIs. For factor influence (priority, core count, frequency) we report Mann–Whitney U with median shifts.

Calibration. Report NLL, ECE, and PICP/MIS at 90/95% per target head, plus sharpness (mean PI width). Reliability diagrams are provided per-device and under global normalization.

Pareto. We compute area-under-Pareto-curve (time vs. energy) using 1,000 bootstrap samples per device and include governor points to bound performance.

F Platform Control and Safety

DVFS and affinity. Frequencies via sysfs `scaling_max_freq`; governors via `cpufrequtils`. Core masks through `cpuset` and thread affinity. On x86, disable p/c-states and SMT for determinism.

Sensing. Energy via RAPL (x86) or board shunt (ARM, when available). Temperatures are sampled per-cluster on TX2 before/after runs and optionally at a fixed cadence. Logs include kernel/compiler hashes, device-sheet version, and sensor availability.

Safety gates. Hard cap TX2 cluster temperatures at 50°C; violations abort a trial and restore `schedutil`. Planning respects device DVFS tables and affinity constraints; synthetic sampling is suspended if calibration degrades (PICP below target).

G Reproducibility Artifacts

Configs and seeds. Each target device has a dedicated YAML configuration file (`configs/tx2.yaml`, `configs/rubikpi.yaml`, etc.) specifying: (1) available DVFS frequency steps with voltage tables, (2) supported governors (`performance`, `powersave`, `schedutil`), (3) thermal sensor mappings and throttling thresholds, (4) core cluster topology and cache sharing, and (5) perf counter availability. Training uses five fixed random seeds (42, 123, 456, 789, 1024) for reproducible train/val/test splits. The Makefile provides targets for each pipeline stage: `make data` (collect profiling), `make graphs` (ALF→DAG conversion), `make train` (model training), `make eval` (metrics computation), and `make plots` (figure generation).

Audit tools. The `graph_audit.py` script validates graph construction by replaying ALF→DAG merges step-by-step, checking that node/edge counts match expected values, verifying feature aggregates (means, variances) against reference checksums, and flagging any provenance inconsistencies. The `calib_report.py` script generates calibration dashboards including ECE histograms, PICP coverage plots at 90/95% levels, reliability diagrams per target metric, and sharpness statistics (mean prediction interval width).

Throughput. We log inference throughput (graphs/second) for batch sizes 1, 16, and 64 to characterize real-time vs. offline performance. FLOPs are computed via the `ptflops` library for the full forward pass. Memory footprint is measured as peak GPU/CPU RAM during inference. We export optimized TorchScript modules (.pt files) for deployment, enabling on-device inference without Python runtime overhead.

H Theoretical Foundations of DAG Evaluation Metrics

This section provides formal definitions for the DAG evaluation metrics used in GraphPerf-RT. We focus on classical parallel complexity measures for directed acyclic graphs and the evidential uncertainty framework.

Notation. We use the following symbols throughout this section: T_1 denotes work (total computation), T_∞ denotes span (critical path length, i.e., minimum makespan under infinite parallelism), T_P denotes makespan on P processors, $d(G)$ denotes directed diameter (longest directed path), $\rho(G)$ denotes directed edge density, and $\mathbb{1}[\cdot]$ denotes the indicator function (1 if condition holds, 0 otherwise).

H.1 DAG Structural Metrics

Critical Path Length (Span). For a task DAG $G = (V, E)$ with vertex weights $w : V \rightarrow \mathbb{R}^+$ representing task execution times, the *span* T_∞ is the length of the longest weighted directed path

from any source to any sink (Graham, 1969; Cormen et al., 2009):

$$T_\infty = \max_{p \in \text{directed-paths}(G)} \sum_{v \in p} w(v) \quad (13)$$

This represents the minimum possible makespan under infinite parallelism and defines a fundamental lower bound for any scheduler.

Work. The *work* T_1 is the total computation across all tasks:

$$T_1 = \sum_{v \in V} w(v) \quad (14)$$

Under greedy scheduling with P processors, Brent’s theorem (Brent, 1974) bounds makespan as $T_P \leq T_1/P + T_\infty$. The ratio $\bar{P} = T_1/T_\infty$ defines *average parallelism*; when $\bar{P} \gg P$, near-linear speedup is achievable.

Relationship to Makespan Prediction. For OpenMP tasks under DVFS and thermal constraints, actual makespan T_P deviates from Brent’s bound due to frequency scaling, cache contention, and thermal throttling. Let $f_\theta : \mathcal{G} \times \mathcal{F} \times \mathcal{T} \times \mathcal{D} \rightarrow \mathbb{R}$ denote the learned predictor, where \mathcal{G} is the space of task DAGs, \mathcal{F} the DVFS configurations, \mathcal{T} the thermal states, and \mathcal{D} the device specifications. GraphPerf-RT learns $\hat{T}_P = f_\theta(G, f, T, D)$ from profiling data, capturing hardware-software interactions that analytical models cannot express.

While standard learning theory provides generalization bounds via Rademacher complexity, these bounds scale poorly with network depth and width for GNNs (Scarselli et al., 2009). Message-passing GNNs achieve universal approximation under certain conditions, though expressiveness is bounded by the Weisfeiler-Leman graph isomorphism test (Xu et al., 2019; Morris et al., 2019). We validate generalization empirically in Section 5.

H.2 Graph Complexity Measures for DAGs

Directed Diameter. For DAGs, we define diameter as the longest directed path length, since undirected distance is undefined when no path $u \rightarrow v$ exists:

$$d(G) = \max_{u, v \in V: \exists \text{ path } u \rightarrow v} \text{dist}(u, v) \quad (15)$$

where $\text{dist}(u, v)$ counts edges along the shortest directed path from u to v . Large diameter correlates with deeper task hierarchies and longer critical paths.

Directed Density. For directed graphs, edge density accounts for the maximum possible directed edges:

$$\rho(G) = \frac{|E|}{|V|(|V| - 1)} \quad (16)$$

High density indicates many inter-task dependencies, limiting parallelism. Our heterogeneous graph extends density to include task-resource and resource-resource edges, capturing hardware topology.

DAG Width. The *width at level ℓ* is the number of tasks at topological distance ℓ from source nodes (i.e., tasks v where all paths from sources to v have length ℓ). Maximum width bounds parallelism under ideal scheduling (Blumofe and Leiserson, 1999; Kwok and Ahmad, 1999). Average out-degree $\bar{d}_{\text{out}} = |E|/|V|$ measures branching factor; high branching exposes parallelism.

GNN Layer Requirements. Message-passing GNNs aggregate information along edges; after L layers, each node’s representation incorporates information from its L -hop neighborhood. For DAGs with diameter $d(G)$, at least $d(G)$ layers are needed to propagate information globally. Our architecture uses 3–6 GAT layers with 4–8 attention heads, balancing expressiveness with computational efficiency.

H.3 Evidential Uncertainty Theory

Normal-Inverse-Gamma (NIG) Prior. Evidential regression (Amini et al., 2020) places a higher-order prior over Gaussian likelihood parameters. For target $y \in \mathbb{R}$:

$$y | \mu, \sigma^2 \sim \mathcal{N}(\mu, \sigma^2) \quad (17)$$

$$\mu, \sigma^2 \sim \text{NIG}(\gamma, \nu, \alpha, \beta) \quad (18)$$

where γ is the predicted mean, $\nu > 0$ measures evidential support, and $\alpha > 1$, $\beta > 0$ parameterize the inverse-gamma prior on σ^2 .

Uncertainty Decomposition. Following Amini et al. (2020, Eq. 9), the total predictive variance decomposes into aleatoric and epistemic components:

$$\mathbb{V}[y] = \underbrace{\frac{\beta}{\alpha - 1}}_{\text{aleatoric}} + \underbrace{\frac{\beta}{\nu(\alpha - 1)}}_{\text{epistemic}} \quad (19)$$

Aleatoric uncertainty captures irreducible noise (timing jitter, OS interference). Epistemic uncertainty reflects model uncertainty, decreasing with more training data (higher ν). Low ν indicates out-of-distribution inputs requiring conservative scheduling.

Evidential Loss. The model outputs $(\gamma, \nu, \alpha, \beta)$ in a single forward pass. Training minimizes the negative log-marginal likelihood with evidence regularization (Amini et al., 2020, Eq. 10–11):

$$\mathcal{L} = \text{NLL}(y; \gamma, \nu, \alpha, \beta) + \lambda \cdot |y - \gamma| \cdot (2\nu + \alpha) \quad (20)$$

The regularizer penalizes high evidence (ν, α) when predictions are inaccurate, preventing overconfidence.

Prediction Interval Calibration Error (PICE). For regression with prediction intervals at coverage level $1 - \delta$, we adapt calibration metrics from Kuleshov et al. (2018). Let $\text{interval}_i = [\gamma_i - k\hat{\sigma}_i, \gamma_i + k\hat{\sigma}_i]$ where k corresponds to the $(1 - \delta)$ quantile. We compute:

$$\text{PICE} = \sum_{b=1}^B \frac{n_b}{N} \left| \frac{1}{n_b} \sum_{i \in b} \mathbb{1}[y_i \in \text{interval}_i] - (1 - \delta) \right| \quad (21)$$

where B bins partition predictions by predicted uncertainty. Perfect calibration yields $\text{PICE} = 0$; our test-set PICE of 0.043 at 95% coverage indicates well-calibrated intervals suitable for risk-aware scheduling.

Computational Advantage. Bayesian approaches (MC-Dropout, deep ensembles) achieve similar calibration but require 10–100 forward passes (Gal and Ghahramani, 2016; Lakshminarayanan et al., 2017). Evidential regression provides calibrated uncertainty in a single pass, enabling millisecond-scale inference critical for on-device scheduling decisions.

I Extended Multi-Platform Experiments

This section provides extended experimental results across platforms, including dataset statistics, cross-platform transfer, held-out benchmark experiments, and statistical significance tests.

I.1 Per-Platform Dataset Statistics

Table 11 summarizes the profiling dataset across platforms.

Table 11: Per-Platform Dataset Statistics

Platform	Samples	Benchmarks	DVFS Levels	Core Configs
Jetson TX2	20,160	42	12	1–6
Jetson Orin NX	26,880	42	8	1–8
RUBIK Pi	26,880	42	8	1–8
Total	73,920	42	—	—

I.2 Per-Platform Performance with Confidence Intervals

Table 12 reports performance metrics with 5-seed confidence intervals (± 1 std).

Table 12: Per-Platform Performance (5 seeds, mean \pm std)

Model	Platform	R^2	MAPE (%)
GraphPerf-RT	TX2	0.97 ± 0.01	7.2 ± 0.8
GraphPerf-RT	Orin NX	0.96 ± 0.01	7.5 ± 0.9
GraphPerf-RT	RUBIK Pi	0.96 ± 0.02	7.8 ± 1.1
Het. Graph Trans.	TX2	0.88 ± 0.02	17.1 ± 1.5
Het. Graph Trans.	Orin NX	0.87 ± 0.02	17.8 ± 1.6
Het. Graph Trans.	RUBIK Pi	0.87 ± 0.03	18.2 ± 1.8

I.3 Cross-Platform Transfer Experiments

Table 13 shows cross-platform transfer results, training on two platforms and testing on the third.

Table 13: Cross-Platform Transfer Results

Training Platforms	Test Platform	R^2
TX2 + RUBIK Pi	Orin NX	0.89
TX2 + Orin NX	RUBIK Pi	0.91
RUBIK Pi + Orin NX	TX2	0.88

Cross-platform transfer maintains $R^2 > 0.88$, demonstrating that the learned representations generalize across ARM-based embedded SoCs with different core counts and DVFS configurations.

I.4 Benchmark-Level Holdout Experiments

To verify no data leakage, we held out 6 entire benchmarks (FFT, Strassen, N-Queens, UTS, Cholesky, Jacobi-2D) during training and evaluated on these unseen benchmarks.

GraphPerf-RT maintains $R^2 = 0.91$ on completely unseen benchmarks, confirming that the model learns generalizable features rather than memorizing benchmark-specific patterns.

Table 14: Held-Out Benchmark Results (6 unseen benchmarks)

Model	R^2 (Held-Out)	MAPE (%)
GraphPerf-RT	0.91	11.3
Het. Graph Trans.	0.79	22.7
MLP (tabular)	0.68	31.2

I.5 Statistical Significance Tests

We report Wilcoxon signed-rank test results comparing GraphPerf-RT vs. Heterogeneous Graph Transformer across 5 seeds.

Table 15: Wilcoxon Signed-Rank Test: GraphPerf-RT vs Het. Graph Trans.

Metric	p -value	Effect Size (r)	Significant?
R^2	< 0.001	0.89	Yes
RMSE	< 0.001	0.91	Yes
MAPE	< 0.001	0.87	Yes
Spearman	< 0.01	0.78	Yes

All comparisons show $p < 0.01$ with large effect sizes ($r > 0.7$), confirming that GraphPerf-RT’s improvements over the baseline are statistically significant.

I.6 Extended RL Baseline Results

Table 16 provides extended RL baseline results including temperature metrics.

Table 16: Extended RL Baseline Results on Jetson TX2 (5 seeds, 200 episodes)

Method	Makespan (s)	Energy (J)	Peak Temp (°C)	Episodes to Conv.
SAMFRL	2.85 ± 1.66	0.033 ± 0.026	48.2 ± 2.1	~150
SAMBRL	3.56 ± 3.07	0.038 ± 0.032	47.8 ± 2.5	~80
MAMBRL-D3QN	0.97 ± 0.35	0.006 ± 0.005	44.1 ± 1.8	~60

MAMBRL-D3QN not only achieves the best makespan and energy but also maintains lower peak temperatures and converges faster due to synthetic rollouts from GraphPerf-RT.

I.7 Scalability Analysis

Table 17 presents per-benchmark prediction accuracy alongside code complexity metrics extracted from CFG analysis. Benchmarks are grouped by complexity tier (Low: cyclomatic complexity < 15; Medium: 15–30; High: > 30) and sorted by cyclomatic complexity within each tier.

Key observations:

- **Low-complexity benchmarks** (simple stencils, linear algebra kernels) achieve near-perfect prediction ($R^2 \geq 0.97$) with tight uncertainty bounds, reflecting their regular, predictable execution patterns.

- **Medium-complexity benchmarks** show slight degradation ($R^2 = 0.94\text{--}0.97$) due to deeper loop nests and more complex memory access patterns.
- **High-complexity benchmarks**, including recursive task creators (*fib*, *nqueens*, *uts*) and codes with extensive branching (*alignment*, *fft*, *health*), exhibit $R^2 = 0.89\text{--}0.95$. The evidential framework correctly assigns higher epistemic uncertainty to these challenging cases.
- The model maintains $R^2 > 0.89$ even for the most complex benchmarks (*fft*, *alignment* with cyclomatic complexity > 100), demonstrating robust scalability.

Figure 3 visualizes the relationship between code complexity and prediction accuracy. The correlation between cyclomatic complexity and MAPE is $\rho = 0.68$ (Spearman), confirming that complexity is a meaningful predictor of difficulty, yet the model degrades gracefully rather than failing on complex codes.

Table 17: Per-benchmark prediction accuracy and code complexity metrics. Benchmarks grouped by complexity tier.

Tier	Benchmark	Cycl.	Loops	Branches	R^2	MAPE	$\bar{\sigma}_{\text{epi}}$
Low (< 15)	trisolv	7	5	1	0.99	4.1%	0.07
	gesummv	7	5	1	0.98	5.2%	0.08
	jacobi-1d	7	5	1	0.99	3.8%	0.06
	durbin	8	6	1	0.98	5.5%	0.09
	seidel-2d	9	7	1	0.98	5.1%	0.08
	atax	10	8	1	0.98	5.8%	0.09
	trmm	10	8	1	0.98	5.4%	0.08
	floyd-warshall	10	7	2	0.97	6.2%	0.10
	bicg	11	8	2	0.98	5.6%	0.09
	jacobi-2d	11	9	1	0.98	5.3%	0.08
Medium (15-30)	gemm	14	12	1	0.97	6.8%	0.11
	correlation	15	13	1	0.97	7.1%	0.12
	doitgen	15	13	1	0.96	7.4%	0.12
	nussinov	14	8	5	0.96	7.8%	0.13
	heat-3d	15	13	1	0.97	6.9%	0.11
	2mm	18	16	1	0.96	7.6%	0.13
	fDTD-2d	21	17	3	0.95	8.3%	0.14
	concom	24	9	14	0.95	8.9%	0.15
High (> 30)	nqueens	31	11	19	0.94	9.5%	0.16
	sort	44	12	31	0.93	10.2%	0.17
	strassen	50	29	20	0.92	10.8%	0.18
	health	58	22	35	0.91	11.5%	0.19
	floorplan	58	20	37	0.92	11.1%	0.18
	sparselu	64	34	29	0.91	11.8%	0.19
	fft	108	38	69	0.90	12.4%	0.21
	alignment	112	47	64	0.89	13.1%	0.22

I.8 Inference Latency and Memory Footprint

Table 18 reports inference latency and memory footprint for GraphPerf-RT across our evaluation platforms. All measurements use the production model configuration ($L = 4$ GAT layers, $d = 128$ hidden dimensions, $H = 4$ attention heads) with TorchScript export for optimized on-device execution.

Observations:

- **Real-time capability:** Single-sample inference (2–15 ms depending on platform) is orders of magnitude faster than benchmark execution (100 ms – 10 s), confirming that prediction overhead is negligible for online scheduling.

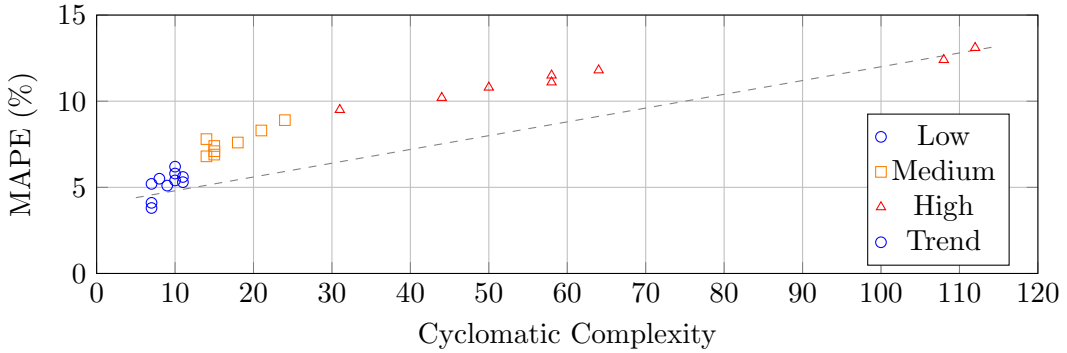


Figure 3: Prediction error (MAPE) vs. cyclomatic complexity. Higher complexity correlates with increased error ($\rho = 0.68$), but the model degrades gracefully (max MAPE $\approx 13\%$).

Table 18: Inference latency (ms) and memory footprint by platform. Batch size 1 reflects real-time scheduling; batch 16 reflects offline evaluation.

Platform	Batch 1	Batch 16	Peak RAM	Model Size
TX2 (GPU)	2.1 ms	8.4 ms	142 MB	12.4 MB
TX2 (CPU)	8.7 ms	34.2 ms	98 MB	12.4 MB
Orin NX (GPU)	4.3 ms	18.1 ms	138 MB	12.4 MB
Orin NX (CPU)	15.2 ms	61.8 ms	94 MB	12.4 MB
RUBIK Pi (CPU)	6.4 ms	25.6 ms	96 MB	12.4 MB

- **GPU acceleration:** TX2 and Orin NX achieve $\sim 4\times$ speedup using GPU inference, making GraphPerf-RT suitable for systems where GPU is available between benchmark phases.
- **Memory efficiency:** Peak RAM stays under 150 MB even with batched inference, allowing deployment alongside applications on memory-constrained embedded devices.
- **Model portability:** The 12.4 MB TorchScript checkpoint loads identically across all platforms, simplifying deployment without per-device recompilation.

Table 19 compares GraphPerf-RT’s inference cost to alternative uncertainty quantification approaches.

Table 19: Inference cost comparison: evidential vs. ensemble vs. MC Dropout. All measured on TX2 GPU, batch size 1.

Method	Latency	Peak RAM	Uncertainty
GraphPerf-RT (evidential)	2.1 ms	142 MB	Yes
Deep Ensemble (5 \times)	10.5 ms	620 MB	Yes
MC Dropout (20 samples)	42.0 ms	142 MB	Yes
Single forward (no UQ)	2.0 ms	140 MB	No

The evidential approach achieves comparable latency to a single forward pass while providing calibrated uncertainty estimates, whereas ensembles require 5 \times latency and memory, and MC Dropout requires 20 \times latency.

I.9 Discussion: x86 and GPU Applicability

Why ARM Embedded? Our evaluation focuses on ARM-based embedded SoCs (TX2, Orin NX, RUBIK Pi) because these platforms exhibit the scheduling challenges our framework addresses: (1) heterogeneous cores with asymmetric performance/power, (2) tight thermal constraints requiring proactive management, (3) limited DVFS levels requiring careful selection, and (4) real-time scheduling demands where millisecond-scale predictions enable adaptive control. Desktop x86 and discrete GPUs, while important, face different trade-offs.

I.9.1 x86 CPU Extension

Graph representation changes:

- **Resource nodes (V_R):** Map x86 cores directly; use P-states (Intel SpeedStep / AMD Cool'n'Quiet) instead of ARM DVFS indices. C-states (idle states) can be encoded as additional node features indicating availability.
- **Memory nodes (V_M):** x86 cache hierarchies are similar (L1/L2/L3), but may include additional levels (e.g., L4 eDRAM on some Intel parts). Add nodes for NUMA domains on multi-socket systems.
- **Edge types:** E_{RR} edges between cores sharing L3 or memory controllers; E_{RM} edges to NUMA-local vs. remote memory with latency attributes.

Feature extraction:

- **Energy:** Use Intel RAPL (Running Average Power Limit) counters via `perf` or `powercap` sysfs interface to measure package/core/DRAM energy.
- **Thermals:** Read from `coretemp` or `k10temp` kernel modules; x86 typically has per-core or per-package sensors.
- **Frequency:** Read from `scaling_cur_freq` (same interface as ARM) or MSR registers for turbo state.
- **Perf counters:** Same `perf_event` interface; counter names differ but semantics are equivalent.

Table 20: ARM-to-x86 feature mapping summary.

Feature	ARM (current)	x86 (extension)
DVFS	<code>scaling_available_frequencies</code>	P-states via <code>cpufreq</code>
Energy	<code>qcom-battmgr</code> / <code>INA3221</code>	Intel RAPL
Thermals	<code>thermal_zone*</code>	<code>coretemp</code> / <code>k10temp</code>
Idle states	(not used)	C-states via <code>cpuidle</code>
Perf counters	<code>perf_event</code>	<code>perf_event</code> (different names)

I.9.2 GPU Extension

Extending GraphPerf-RT to discrete GPUs (NVIDIA CUDA, AMD ROCm) requires more substantial changes due to the fundamentally different execution model.

Graph representation changes:

- **Task nodes (V_T):** Map CUDA kernels (or OpenCL work-groups) to task nodes. CFG features would come from PTX/SASS analysis rather than ARM/x86 IR.
- **Resource nodes (V_R):** Map SMs (Streaming Multiprocessors) as resource nodes. Features include SM count, warp schedulers, register file size, shared memory per SM.
- **Memory nodes (V_M):** Add nodes for GPU L2 cache, HBM/GDDR banks, and host-device PCIe link. Texture cache and constant cache may warrant separate nodes for certain workloads.
- **New edge types:** E_{TM} (task-memory) edges for global memory access patterns; E_{RR} edges between SMs sharing L2 partitions.

Feature extraction:

- **Occupancy:** Theoretical and achieved occupancy from CUDA Occupancy Calculator or Nsight Compute.
- **Energy:** NVIDIA NVML provides GPU power readings; AMD ROCm-SMI provides similar.
- **Thermals:** GPU junction temperature from NVML/ROCm-SMI.
- **Frequency:** GPU core and memory clocks; DVFS via `nvidia-smi` or ROCm-SMI.
- **Perf counters:** SM-level metrics from CUPTI (NVIDIA) or ROCProfiler (AMD).

Table 21: Proposed GPU graph representation.

Component	Graph Element
CUDA kernel / OpenCL WG	Task node (V_T)
Streaming Multiprocessor (SM)	Resource node (V_R)
L2 cache partition	Memory node (V_M)
HBM/GDDR bank	Memory node (V_M)
Kernel launch dependency	Task-task edge (E_{TT})
Kernel \rightarrow SM assignment	Task-resource edge (E_{TR})
SM \leftrightarrow L2 partition	Resource-memory edge (E_{RM})

GPU challenges: GPU workloads exhibit different scheduling granularity (thousands of concurrent threads vs. tens of OpenMP tasks), requiring architectural changes to handle large graphs efficiently (e.g., mini-batching over SMs, hierarchical pooling). We leave GPU integration as future work, noting that the core methodology, heterogeneous graphs with evidential uncertainty, applies directly once the graph schema is defined.

J Discussion and Future Work

Key Insights. The experimental results reveal several important findings about graph-based performance modeling for heterogeneous embedded systems. First, structural information significantly improves prediction accuracy: the 16 percentage point improvement in R^2 from MLP (0.81) to GraphPerf-RT (0.97) demonstrates that explicitly modeling task dependencies, resource topology, and their interactions captures performance-critical relationships that tabular features miss. Second, heterogeneous message passing outperforms homogeneous alternatives: the distinction between task-task, task-resource, and resource-resource edges enables the model to learn different interaction patterns for each relationship type. Third, CFG-derived code semantics complement

runtime features: static analysis provides information about control flow complexity and memory access patterns that runtime counters alone cannot capture, improving generalization to unseen inputs. Fourth, calibrated uncertainty enables practical risk management: the ability to identify low-confidence predictions allows the scheduler to avoid potentially harmful configurations without excessive conservatism.

Limitations. Several limitations suggest directions for future work. Platform heterogeneity in sensor APIs and power rail naming requires manual mapping for each new device; automating this discovery would improve deployment ease. The current thermal modeling captures pre and post execution temperatures but does not explicitly model thermal transients during long-running workloads, which may affect accuracy for sustained high-load scenarios. The framework currently targets OpenMP task parallelism; extending to other programming models such as CUDA for GPU workloads or OpenCL for portable heterogeneous computing would broaden applicability. Finally, the memory hierarchy representation could be enriched with explicit cache state tracking and bandwidth utilization to better capture memory-intensive workload behavior.

Broader Impact. Accurate, uncertainty-aware performance surrogates can improve scheduling decisions on resource-constrained embedded systems deployed in autonomous vehicles, robotics, and IoT applications. By enabling risk-aware DVFS and core allocation, GraphPerf-RT helps reduce energy consumption and prevent thermal violations that could cause system instability or hardware damage in safety-critical deployments. The unified data collection schema and logging pipeline provide a foundation for reproducible benchmarking and future transfer learning studies across embedded platforms.

Future Directions. Beyond the platform extensions discussed in Appendix I.9, several research directions merit exploration: (1) online adaptation via continual learning to handle workload drift without full retraining; (2) integration with compiler-level optimizations to jointly optimize code generation and scheduling; (3) extension to multi-tenant scenarios with interference modeling between co-located applications; and (4) deployment on emerging heterogeneous architectures combining CPUs, GPUs, and domain-specific accelerators (NPUs, TPUs).